HHS Public Access

Author manuscript

Cell. Author manuscript; available in PMC 2022 January 21.

Published in final edited form as:

Cell. 2021 January 21; 184(2): 384–403.e21. doi:10.1016/j.cell.2020.12.031.

Spliceosome-Targeted Therapies Trigger an Antiviral Immune Response in Triple-Negative Breast Cancer

Elizabeth A. Bowling[1,10], **Jarey H. Wang**[1,2,10], **Fade Gong**[1], **William Wu**[1,2], **Nicholas J. Neill**[3], **Ik Sun Kim**[4], **Siddhartha Tyagi**[1], **Mayra Orellana**[1], **Sarah J. Kurley**[1], **Rocio Dominguez-Vidaña**[3], **Hsiang-Ching Chung**[1], **Tiffany Y.-T. Hsu**[1,2], **Julien Dubrulle**[5], **Alexander B. Saltzman**[1], **Heyuan Li**[1], **Jitendra K. Meena**[1], **Gino M. Canlas**[1,6], **Srinivas Chamakuri**[6], **Swarnima Singh**[4], **Lukas M. Simon**[7], **Calla M. Olson**[7], **Lacey E. Dobrolecki**[4], **Michael T. Lewis**[4,5,8], **Bing Zhang**[3,4,8], **Ido Golding**[1], **Jeffrey M. Rosen**[5,8], **Damian W. Young**[6,7], **Anna Malovannaya**[1], **Fabio Stossi**[5], **George Miles**[4,5], **Matthew J. Ellis**[4,5], **Lihua Yu**[9], **Silvia Buonamici**[9], **Charles Y. Lin**[3,7,8], **Kristen L. Karlin**[7], **Xiang H.-F. Zhang**[4,8], **Thomas F. Westbrook**[1,3,4,5,7,11,*]

[1.]Verna and Marrs McLean Department of Biochemistry and Molecular Biology, Baylor College of Medicine, Houston, TX, 77030, USA

[2.]Medical Scientist Training Program, Baylor College of Medicine, Houston, TX, 77030, USA

[3.]Department of Molecular and Human Genetics, Baylor College of Medicine, Houston, TX,77030, USA

[4.]Lester and Sue Smith Breast Center, Baylor College of Medicine, Houston, TX, 77030, USA

[5.]Department of Molecular and Cellular Biology, Baylor College of Medicine, Houston, TX,77030, USA

[6.]Department of Pharmacology and Chemical Biology, Baylor College of Medicine, Houston, TX, 77030, USA

[*]Correspondence: thomasw@bcm.edu.

[10]These authors contributed equally

[11]Lead Contact

Author Contributions

Conceptualization, E.A.B, J.H.W., X.H.-F.Z., and T.F.W.

Methodology, E.A.B., J.H.W., F.G., N.J.N., I.S.K., J.D., and K.L.K.

Software, J.H.W., N.J.N., R.D.-V., J.D., B.Z., C.Y.L., and T.F.W.

Formal Analysis, J.H.W., N.J.N., R.D.-V., C.Y.L., and T.F.W.

Investigation, E.A.B., J.H.W., F.G., W.W., N.J.N., I.S.K., S.T., M.O., S.J.K., H.-C.C., T.Y.-T.H., A.B.S., H.L., J.K.M., G.M.C., S.C., S.S., G.M., and K.L.K.

Resources, L.M.S, C.M.O, L.E.D., I.G., J.M.R., D.W.Y., A.M., F.S., M.T.L., G.M., M.J.E., L.Y., S.B., C.Y.L., K.L.K., X.H.-F.Z., and T.F.W.

Writing –Original Draft, E.A.B., J.H.W., T.F.W.

Funding Acquisition, X.H.-F.Z., and T.F.W.

Declaration of Interests

The authors declare no competing interests.

Spliceosome inhibitors generate intron-retaining mis-spliced RNAs then activate downstream antiviral signaling and apoptosis in tumors in mouse models of breast cancer.

[7]Therapeutic Innovation Center, Baylor College of Medicine, Houston, TX, 77030, USA

[8]Dan L. Duncan Cancer Center, Baylor College of Medicine, Houston, TX, 77030, USA

[9]H3Biomedicine, Cambridge, MA, 02139, USA

SUMMARY

Many oncogenic insults deregulate RNA splicing, often leading to hypersensitivity of tumors to spliceosome-targeted therapies (STTs). However, the mechanisms by which STTs selectively kill cancers remain largely unknown. Herein, we discover that mis-spliced RNA itself is a molecular trigger for tumor killing through viral mimicry. In MYC-driven triple-negative breast cancer, STTs cause widespread cytoplasmic accumulation of mis-spliced mRNAs, many of which form double-stranded structures. Double-stranded RNA (dsRNA)-binding proteins recognize these endogenous dsRNAs, triggering antiviral signaling and extrinsic apoptosis. In immune-competent models of breast cancer, STTs cause tumor cell-intrinsic antiviral signaling, downstream adaptive immune signaling, and tumor cell death. Furthermore, RNA mis-splicing in human breast cancers correlates with innate and adaptive immune signatures, especially in MYC-amplified tumors that are typically immune-cold. These findings indicate that dsRNA-sensing pathways respond to global aberrations of RNA splicing in cancer and provoke the hypothesis that STTs may provide unexplored strategies to activate anti-tumor immune pathways.

Graphical Abstract

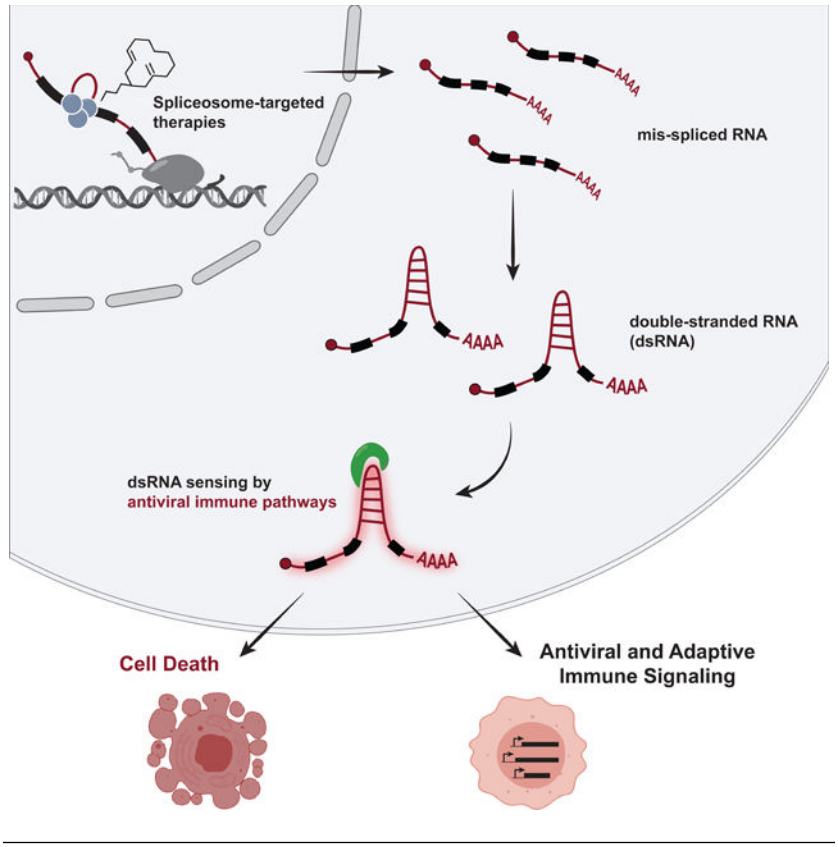

INTRODUCTION

Tumor transcriptomes are replete with indications of deregulated RNA splicing, such as aberrant retention of introns and alterations in both canonical and alternative splicing (Venables, 2004; Zhang and Manley, 2013; Dvinge and Bradley, 2015; Kahles *et al.*, 2018). Many tumor features contribute to this deregulation, including recurrent mutations to RNA splicing factors in both solid and hematologic malignancies (Darman et al., 2015; DeBoever et al., 2015; Graubert et al., 2012; E. Kim et al., 2015; Seiler et al., 2018a; Wang et al., 2016; Zhang et al., 2015). Non-spliceosome-associated oncogenic alterations, such as hyperactivation of the transcription factor MYC, have also been shown to broadly deregulate splicing and lead to increased reliance on components of pre-mRNA splicing (David *et al.*, 2010; Das *et al.*, 2012; Hubert *et al.*, 2013; Hsu *et al.*, 2015; Koh *et al.*, 2015), in part through elevated synthesis of pre-mRNA and consequent burden on the spliceosome. As a result, cancers driven by MYC, spliceosome mutations, and other oncogenic events are highly sensitive to further genetic and pharmacologic perturbations of the spliceosome (Chan et al., 2017; Hsu et al., 2015; Hubert et al., 2013; Koh et al., 2015; Lee et al., 2016; Obeng et al., 2016; Seiler et al., 2018b; Shirai et al., 2017). This has led to clinical evaluation of small molecule spliceosome modulators in patients (NCT02841540), the development of additional classes of therapeutics targeting the spliceosome (Berg *et al.*, 2012; Pawellek *et al.*, 2014; Han *et al.*, 2017; Sidarovich *et al.*, 2017; Uehara *et al.*, 2017), and the study of spliceosome-targeted therapies in aggressive and poor prognosis tumors that lack targeted therapy options, like triple-negative breast cancer (TNBC).

Small molecule splicing modulators have been explored as anti-cancer therapeutics for over 20 years (Nakajima *et al.*, 1996; Kaida *et al.*, 2007), but their downstream mechanisms of selective anti-tumor activity are not well understood. While spliceosome modulators are known to induce transcriptome-wide mis-splicing, previous work has focused on mis-splicing of specific genes to explain tumor cell death and other phenotypes associated with splicing perturbation. For instance, cell cycle arrest phenotypes have been attributed to mis-splicing of genes encoding cell cycle regulators such as p27 (Kaida *et al.*, 2007; Yoshimoto *et al.*, 2017), Mdm4 (Bezzi *et al.*, 2013), or cell division cycle (CDC) proteins (Hubert *et al.*, 2013). Likewise, alternative splicing of BCL2 family genes is thought to induce activation of apoptosis in some contexts (Aird et al., 2019; Larrayoz et al., 2016; Moore et al., 2010). These important studies highlight the impact of individual mis-spliced mRNAs and their encoded proteins, but also emphasize that culprit mis-spliced genes may vary widely across individual tumors and their diverse transcriptomes. This leaves open the question of whether there are more generalized pathways that govern tumor cell response to spliceosome-targeted therapies (STTs), especially in tumor types that exhibit heightened dependency on RNA splicing.

The current study reveals that mis-spliced mRNAs themselves are a class of macromolecules that are sensed upon spliceosome inhibition, triggering an antiviral immune response and TNBC cell death. We show that STTs cause widespread accumulation of intron-containing transcripts and double-stranded RNA (dsRNA) in the cytoplasm of TNBC cells. These endogenous intron-containing dsRNAs trigger an antiviral immune response via multiple dsRNA binding proteins, including those that activate the signaling integrator MAVS.

Notably, STTs trigger both tumor cell-intrinsic antiviral signaling and adaptive immune signaling in animal models of breast cancer. Moreover, intrinsic defects in RNA splicing in primary human breast malignancies correlate with evidence of immune engagement and associate with improved disease-free survival in breast cancer patients. These findings point to dysregulated splicing as an unanticipated approach by which to trigger tumor-intrinsic dsRNA antiviral signaling, and provide mechanistic insight to explain, in part, the selective anti-cancer activity of STTs.

RESULTS

Spliceosome-Targeted Therapies Stimulate Antiviral Signaling in MYC-Driven Triple-Negative Breast Cancer

Previous studies have demonstrated that MYC-driven cancers such as triple-negative breast cancer (TNBC) are sensitive to partial pharmacologic and genetic perturbation of the spliceosome (Hsu *et al.*, 2015; Koh *et al.*, 2015). However, the pathways that are activated by and coordinate cell fate decision-making in response to spliceosome inhibition are largely unknown. We integrated two unbiased approaches –gene expression analysis and forward genetic screening –to investigate these pathways. First, we characterized the transcriptional changes of two MYC-driven TNBC cell lines, SUM159 and MDA-MB-231-LM2 (LM2) (Kessler *et al.*, 2012; Hsu *et al.*, 2015), following treatment with the small molecule spliceosome modulator sudemycin D6 (SD6) (Lagisetti *et al.*, 2013) (Figure 1A). Gene set enrichment analysis (GSEA) (Subramanian *et al.*, 2005) revealed that transcriptional changes in response to spliceosome inhibition were highly correlated between the two cell lines (Figure 1B), suggesting that a common set of cellular pathways may respond to acute splicing perturbation. Consistent with previous reports, cell cycle and RNA processing pathways were downregulated in response to spliceosome inhibition (Hsu et al., 2015; Hubert et al., 2013; Seiler et al., 2018b). Surprisingly, immune signaling pathways, including interferon alpha and beta signaling, were among the most significant positively enriched pathways (Figure 1C). Upregulation of both interferon-stimulated genes (e.g. *OAS1, MX1*) and NF-kB responsive genes (e.g. *TNF*, *IL1B)* indicate activation of an antiviral transcriptional program in response to spliceosome inhibition (Figure 1D). Induction of *IFNB* expression preceded the expression of well-characterized interferon-responsive genes, suggesting activation of IFN-responsive antiviral signaling (Figure S1A). These results are not unique to SD6, as treatment of SUM159 and LM2 cells with H3B-8800 (Seiler et al., 2018b), a structurally distinct spliceosome modulator currently in clinical trials (NCT02841540), resulted in similar upregulation of an antiviral transcriptional program of mRNAs (Figure 1E, Figures S1B and S1C) and secretion of their encoded proteins (Figure 1F). Together, these data support the model that inhibition of splicing induces an antiviral immune transcriptional response.

Notably, H3B-8800 induced antiviral transcriptional programs in MYC-driven TNBC cells to a much greater extent than non-transformed mammary epithelial cells (Figure 1E). Given that MYC hyperactivation has been shown to increase sensitivity to spliceosome inhibition, we asked whether MYC hyperactivation alone is sufficient to prime activation of such antiviral programs upon spliceosome inhibition using human mammary epithelial

cells engineered with inducible MYC-ER transgene (MYC-ER HME1) (Hsu et al., 2015; Kessler et al., 2012). Strikingly, the combination of MYC hyperactivation and H3B-8800 treatment induced robust activation of antiviral signaling programs (Figures 1G and 1H), but the individual perturbations did not, strongly suggesting that oncogenic MYC can prime antiviral immune response to spliceosome inhibition.

To confirm that activation of antiviral transcriptional signaling was due to on-target inhibition of spliceosome activity, we evaluated the effects of chemical-genetic depletion of SF3B1, the protein target of SD6 and H3B-8800. Expression of *SF3B1-FKBP12*^{F36V} in SUM159 cells with knockout of endogenous *SF3B1* enabled selective and dose-dependent perturbation of SF3B1 function (Figure S1D; (Nabet *et al.*, 2018)). Similar to treatment with STTs, degradation of SF3B1-FKBP12^{F36V} induced expression of IFN and NF-kB responsive genes (Figures 1I and 1J). From these data, we conclude that spliceosome perturbation induces an antiviral transcriptional response in MYC-driven TNBCs.

Components of Antiviral Response Pathways Modulate Sensitivity to Spliceosome Inhibition Second, we sought to identify genes required for sensitivity to spliceosome inhibition in TNBC cells. We performed a forward genetic screen with a shRNA library (18,370 shRNAs targeting 1,837 genes) targeting signal transducing protein classes (kinases, phosphatases, and ubiquitin ligases). SUM159 cells transduced with the retroviral shRNA library were grown in the presence or absence of SD6 (Figure 2A). The shRNA abundance in tumor cell genomic DNA was quantified in initial and treated samples by sequencing. We focused our downstream analysis on shRNAs that increased in abundance specifically in the SD6-treated state, referred to as “resistance candidates” because candidate knockdown conferred resistance to spliceosome inhibition (Table S1). MeSH term enrichment analysis (Yu, 2018) of the top 50 resistance candidates revealed a cluster of genes involved in immune response (Figure 2B, Table S2), suggesting that immune pathways may regulate tumor cell response to spliceosome-targeted therapies (STTs). StringDB analysis of resistance candidates revealed enrichment of pathways related to immunity and regulation of signaling downstream of double-stranded RNA (dsRNA) sensing (Figure S2A). Notably, 5 of the top 30 resistance candidates were documented modulators of dsRNA-sensing pathways (Figure S2B) (Arimoto *et al.*, 2007; Zeng *et al.*, 2009; Mallampalli *et al.*, 2013; Li *et al.*, 2015; Song *et al.*, 2016; Yu *et al.*, 2017). shRNAs targeting these modulators were consistently enriched upon partial spliceosome inhibition (Figure 2C, Figures S2C and S2D). These data suggest that activation of dsRNA sensing and signaling pathways contributes to sensitivity to spliceosome inhibition. Indeed, independent competition-based assays validated that depletion of *RNF128*, *RNF125*, and *UBE2D1* increased resistance to spliceosome inhibition (Figure 2D, Figures S2E–S2G). As these genes have been shown to mediate activation of antiviral transcriptional programs, we tested whether their depletion would suppress antiviral immune transcriptional activation induced by spliceosome inhibition. Knockout of *RNF128* suppressed induction of immune signaling transcriptional changes upon treatment with SD6 (Figure 2E). Collectively, these unbiased transcriptomic and genetic approaches suggest that partial inhibition of the spliceosome induces antiviral signaling in tumor cells, and that these pathways regulate tumor cell survival in response to STTs.

Spliceosome-Targeted Therapies Cause Cytoplasmic Accumulation of Double-Stranded RNA in TNBC Cells

We next investigated the trigger of antiviral signaling in response to spliceosome inhibition. Our genetic screen indicated that dsRNA antiviral signaling pathways modulate cancer cell response to STTs, suggesting that spliceosome perturbation may lead to accumulation of dsRNA. Immunofluorescence staining using a dsRNA-specific antibody (J2 antibody) (Schönborn *et al.*, 1991) across multiple TNBC lines revealed that H3B-8800 induced significant increases in cytoplasmic dsRNA (Figures 3A–3D, Figures S3A and S3B). The J2 signal was abolished by dsRNA-specific RNase III treatment, indicating that the J2 antibody specifically recognized accumulation of dsRNA structures (Figures 3A–3D). In contrast to these MYC-driven TNBC models, non-transformed HME1 cells did not exhibit increased J2 signal at the same dose of H3B-8800 (Figure S3C). Notably, in the MYC-ER HME1 system, the combination of MYC hyperactivation and H3B-8800 led to a significant increase in dsRNA accumulation compared to MYC or H3B-8800 alone (Figure 3E), indicating that MYC is sufficient to prime accumulation of dsRNAs in response to spliceosome inhibition. Importantly, in both the TNBC and MYC-ER HME1 experimental systems, dsRNA accumulated prominently in the cytoplasm (representative images in Figures 3A, 3C and 3E, Figures S3A and S3B), where dsRNA sensing proteins have been shown to engage dsRNA viruses and other dsRNA species.

Next, we established that direct perturbation of the spliceosome induced dsRNA accumulation. Degradation of exogenous SF3B1-FKBP12^{F36V} in an endogenous *SF3B1* knockout background resulted in accumulation of cytoplasmic dsRNA (Figure 3F), phenocopying the effect of H3B-8800. To further confirm SF3B1-on-target effect of H3B-8800 as the source of dsRNA accumulation, we utilized exogenously expressed *SF3B1*^{R1074H} (Figures S3D and S3G), which confers resistance to small molecules targeting SF3B1 (Seiler et al., 2018b; Yokoi et al., 2011) (Figure S3E and S3H). *SF3B1*^{R1074H} expression suppressed H3B-8800-induced intron retention (Figure S3F) and increase in J2 signal (Figure 3G, Figure S3I). These results indicate that spliceosome inhibition leads to widespread accumulation of cytoplasmic dsRNA in MYC-driven TNBC cells. Together with activation of antiviral signaling by spliceosome inhibition (Figures 1 and 2), these observations support the model that STTs exert a therapeutic effect, at least in part, via dsRNA-sensing and downstream antiviral signaling.

Intron-Retained RNAs Accumulate in the Cytoplasm and Form dsRNA in Response to Spliceosome-Targeted Therapies

We then sought to investigate the source of cytoplasmic dsRNA in response to acute spliceosome inhibition. Spliceosome perturbations induce transcriptome-wide defects in splicing, including intron retention, but the extent to which these intron-retained transcripts are exported and accumulate in the cytoplasm is unclear. Some intron-containing gene isoforms have well-characterized biological functions in the cytoplasm (Buckley et al., 2014), and certain cancer-associated neoepitopes are derived from intron-retained RNA (Smart et al., 2018). However, the majority of intron-retained RNAs are predicted to be degraded by quality control mechanisms (Braunschweig et al., 2014; Doma and Parker, 2007; Popp and Maquat, 2013; Wong et al., 2013; Zhang and Manley, 2013). Surprisingly,

we found that acute spliceosome perturbation led to widespread accumulation of intron-retained transcripts in the cytoplasm of TNBC cells. Poly (A) RNA-seq of cytoplasmic fraction RNA of SUM159 cells treated with H3B-8800 (Figure S4A) revealed a significant increase in intron retention (IR) across 24,883 introns (Figure 4A, Figure S4B). Investigation of individual RNA localization using RNA fluorescence *in situ* hybridization (FISH) revealed a significant increase in intron-containing RNA in the cytoplasm after H3B-8800 treatment (Figures 4B and 4C, Figures S4C–S4F). Importantly, overlapping intronic and exonic foci indicates these cytoplasmic introns are present in the context of unspliced transcripts, as opposed to intron lariats or off-target probe recognition. Based on these results, we conclude that acute spliceosome inhibition induces global accumulation of mis-spliced, intron-containing RNA in the cytoplasm.

Given that spliceosome inhibition induced substantial accumulation of cytoplasmic intron-retained RNAs and dsRNA, we hypothesized that intron-retained mRNAs were a source of cytoplasmic dsRNA. Previous studies have shown that introns form double-stranded structures in the nucleus (Saldi et al., 2014; Sun et al., 2019) and that a large proportion of retrotransposable elements (e.g. LINE, SINE/Alus) in the genome are located in introns (Sela *et al.*, 2007). Notably, there was a significant increase in expression of over 9,000 intron-residing retrotransposons, including LINE and SINE/Alu elements, after H3B-8800 treatment (Figure 4D, Figure S4G). In contrast, expression of retrotransposons residing outside of intronic regions did not substantively change (Figure 4E, Figure S4H). Therefore, in contrast to primarily intergenic endogenous retroviral elements induced by DNA demethylating agents (Chiappinelli et al., 2015; Mehdipour et al., 2020; Roulois et al., 2015), we conclude that acute perturbation of splicing reveals a previously unexplored class of endogenous double-stranded RNAs that may serve as triggers of an antiviral response.

To directly assess the composition of dsRNAs that accumulate after spliceosome inhibition, we performed dsRNA immunoprecipitation using the J2 antibody followed by poly (A) RNA-seq (J2 dsRIP-seq). Introns retained after spliceosome inhibition were significantly enriched by J2 dsRIP-seq (Figures 4F and 4G), suggesting pervasive formation of double-stranded secondary structure. Among those genes with highly J2-enriched retained introns was *RPL30* (Figure 4H), which contains inverted Alu elements that contribute to a long stretch of predicted dsRNA structure (Figure S4I). Interestingly, introns without retrotransposons were also enriched by J2 and predicted to form lengthy, continuous double-stranded structures (Figures S4J and S4K), suggesting that introns broadly contribute to accumulation of dsRNA. Probing of RNA structure using ssRNA digestion followed by RT-qPCR revealed J2-enriched introns were enriched 10–15 fold for dsRNA structure (Figure 4I), supporting their contribution to the pool of dsRNA following spliceosome inhibition. Collectively, these data support the hypothesis that spliceosome inhibition causes accumulation of intron-retained RNAs, which form double-stranded structures that accumulate in the cytoplasm.

Spliceosome-Targeted Therapies Activate Extrinsic Apoptosis via Antiviral dsRNA Sensing Pathways

Our data thus far indicate that STTs cause cytoplasmic accumulation of dsRNA in MYC-driven TNBC. Recognition of cytoplasmic dsRNA has been shown to activate an antiviral transcriptional response, and in some contexts, induce extrinsic apoptosis (Kibler *et al.*, 1997; Gil and Esteban, 2000; Iordanov *et al.*, 2005; Takahashi *et al.*, 2006; Sears *et al.*, 2011; El Maadidi *et al.*, 2014). However, previous work has suggested that STTs induce apoptosis through alternative splicing of BCL2 family genes (Larrayoz et al., 2016; Moore et al., 2010), which mediate the intrinsic apoptotic pathway (Elmore, 2007). Thus, we sought to determine whether extrinsic or intrinsic pathways drive apoptosis in response to STTs. Consistent with prior studies, both H3B-8800 and SD6 activated downstream effector caspases-3 and −7 (Figure 5A, Figure S5A). Notably, both STTs activated caspase-8 (Figure 5B, Figure S5B), an initiator caspase of extrinsic apoptosis. Likewise, in MYC-ER HME1 cells, the combination of MYC hyperactivation and H3B-8800 led to robust induction of both caspases-3 and −7 and caspase-8 activity (Figures S5C and S5D). Additionally, expression of $SF3B1^{R1074H}$ suppressed activation of both caspase-8 and caspases-3 and −7, suggesting that apoptotic cell death is indeed due to on-target spliceosome inhibition (Figure S5E and S5F). Caspase-8 cleavage occurred within 12 hours, preceding caspase-3 cleavage (Figure 5C). Strikingly, inhibition of both caspase-8 and 10, initiators of extrinsic apoptosis, suppressed activation of downstream effector caspases by H3B-8800 and SD6 (Figure 5D, Figure S5G). In contrast, inhibition of caspase-9, an initiator of intrinsic apoptosis, did not significantly suppress caspase-3 and −7 activation (Figure S5G), suggesting intrinsic mechanisms do not play a primary role in activation of apoptosis, at least in the context of TNBC. Additionally, necroptosis is not a primary pathway of cell death as inhibition of RIPK3 did not impede H3B-8800-induced cell death (Figure S5H–S5J). Together, these results indicate that the induction of apoptosis by spliceosome inhibition occurs through extrinsic mechanisms in breast cancer.

Extrinsic apoptosis can be activated through mechanisms that are dependent on cell surface death receptors. We observed that after H3B-8800, death receptor related ligands and receptors were not substantially upregulated (Figures S5K–S5N). Additionally, cFLIP splicing and isoform expression was not changed (Figures S5O and S5P). Knockdown of TNFR1 did not significantly suppress induction of apoptosis (Figures S5Q–S5S). These data suggest that extrinsic apoptosis is activated in a death receptor-independent manner.

Prior studies have shown that recognition of cytoplasmic dsRNA can trigger death receptor-independent extrinsic apoptosis (Gil and Esteban, 2000; El Maadidi *et al.*, 2014). Our genetic screen (Figure 2) implicated the RIG-I-like Receptor (RLR) dsRNA sensing pathway in sensitivity to STTs, suggesting that spliceosome inhibition activates extrinsic apoptosis via dsRNA binding proteins, including RLRs. While there are several dsRNA sensors in the human proteome (Andrejeva et al., 2004; Kang et al., 2002; Liu et al., 2014; Sumpter et al., 2005; Yoneyama et al., 2004; Zhang et al., 2011a, 2011b), their potential redundancy in sensing endogenous dsRNAs and/or stimulating cell death is poorly understood. To systematically test their role in H3B-8800-induced extrinsic apoptosis, we depleted individual dsRNA binding proteins, including RLRs, using multiple

independent siRNAs (Figure S5T) and tested STT-induced extrinsic apoptosis. Depletion of several dsRNA binding proteins partially suppressed activity of caspase-8 and downstream activation of apoptosis upon H3B-8800 treatment (Figures 5E and 5F), while knockdown of others had no effect, suggesting there may be selectivity of dsRNA sensors that recognize endogenous dsRNA accumulation and stimulate apoptosis. The observation that RIG-I and MDA5, which recognize distinct pools of dsRNA (Hornung *et al.*, 2006; Kato *et al.*, 2008; Schmidt *et al.*, 2009; Goubau *et al.*, 2014; Linehan *et al.*, 2018), both contribute to apoptosis suggests diversity in the types of dsRNA that accumulate upon spliceosome perturbation. Collectively, these results indicate that recognition of dsRNAs induced by STTs contributes to downstream activation of apoptosis. However, the observed partial suppression of extrinsic apoptosis suggests there may be redundancy in dsRNA-recognition pathways or that other pathways contribute to apoptosis.

Several of these dsRNA sensors (MDA5, RIG-I, DHX9, and DHX33) converge on activation of the mitochondrial antiviral-signaling protein (MAVS) to induce two independent arms of downstream antiviral signal transduction: transcriptional changes and induction of apoptosis (Kawai et al., 2005; Lei et al., 2009; Liu et al., 2014; Meylan et al., 2005; Seth et al., 2005; Xu et al., 2005; Zhang et al., 2011b). We hypothesized that spliceosome inhibition activates the signaling integrator MAVS, resulting in initiation of an antiviral response. Activation of MAVS results in its aggregation on the mitochondrial membrane (Hou *et al.*, 2011). Indeed, H3B-8800 induced aggregation of MAVS in both SUM159 and LM2 cells, as assessed by immunofluorescence imaging (Figures 5G and 5H, Figures S5U and S5V) and SDD-AGE followed by immunoblotting (Figures 5I and S5W). Knockdown of *MAVS* partially suppressed extrinsic apoptosis (Figures 5J and 5K, Figure S5X). The observed partial suppression of extrinsic apoptosis suggests there may be additional pathways that initiate extrinsic apoptosis. Consistent with this, the dsRNA-sensors DHX36, DDX21, and DDX1 are partially required for H3B-8800-induced extrinsic apoptosis, but have not, to our knowledge, been characterized to signal through MAVS. Finally, knock-out of *MAVS* impaired antiviral transcriptional changes upon H3B-8800 treatment (Figure 5L, Figures S5Y and S5Z). Taken together, these data support the model that STTs induce accumulation of dsRNA and consequently activate dsRNA-sensing pathways (likely MAVS-dependent and –independent), leading to upregulation of an antiviral transcriptional program and activation of extrinsic apoptosis.

RNA Splicing Inhibition Induces Antiviral and Adaptive Immune Signaling in Immune-Competent Models of Breast Cancer

Antiviral signaling through dsRNA pathways induces tumor cell death through a variety of mechanisms, including cell autonomous apoptosis (Der *et al.*, 1997; Kibler *et al.*, 1997) as well as production of cytokines and type 1 IFNs that recruit an adaptive immune response (Chiappinelli *et al.*, 2015; Roulois *et al.*, 2015; Topper *et al.*, 2017; Elion *et al.*, 2018; Ishizuka *et al.*, 2019). While STTs trigger tumor cell death in a cell autonomous manner (Figure 5), robust induction of antiviral transcriptional programs by STTs prompts the hypothesis that such antiviral signaling may also serve as a beacon for downstream host immune surveillance. Therefore, we assessed the impact of spliceosome inhibition on TNBC in an immune-competent host using multiple transplantable syngeneic murine tumor

models (2208L, PyMT-M, AT3, and T11). Consistent with prior work (Seiler et al., 2018b), H3B-8800 treatment was well tolerated. Notably, the effect of spliceosome perturbation on tumor progression varied significantly across these models. H3B-8800 significantly impaired tumor progression in 2208L and PyMT-M tumor models ("sensitive" models), while only modestly delaying tumor growth in AT3 and T11 models ("resistant" models) (Figure 6A), indicating H3B-8800 is differentially efficacious as a single agent across TNBC models.

To investigate the mechanisms contributing to this differential sensitivity, we performed bulk tumor RNA sequencing. Splicing analysis showed that H3B-8800 induced widespread IR across all models. Notably, H3B-8800 induced a significantly greater increase in global IR in sensitive tumor models (Figure 6B) compared to resistant tumor models. The underlying causes of the increased global intron retention in sensitive models are currently unknown, but could be a consequence of multiple mechanisms including partial defects in spliceosome function (e.g. somatic spliceosome mutations (Lee et al., 2016; Obeng et al., 2016; Seiler et al., 2018b; Shirai et al., 2017), increased global transcription rates and corresponding burden on pre-mRNA splicing machinery (e.g. MYC hyperactivation (Hsu et al., 2015; Lin et al., 2012)), impaired quality control of mis-spliced mRNA (e.g. defects in NMD), or other forms of deregulation in RNA processing. Nonetheless, this observation indicates that elevated levels of intron-retained mRNA correlates with efficacy of spliceosome-targeted therapy in these immune-competent models of TNBC.

To further study the underlying causes for differential sensitivity, we queried the differential effects of H3B-8800 on transcriptional programs in sensitive versus resistant models using a DESeq2 multifactor model (Love et al., 2014) followed by enrichment analysis. Pathways upregulated in sensitive models were almost exclusively immune-related pathways, in particular those related to antiviral signaling, cytokine and chemokine signaling, and adaptive immunity (Figures S6A and S6B). H3B-8800 significantly upregulated expression of antiviral signaling genes in sensitive models, which had greater induction of IR, but not in resistant models (Figure 6C). As an orthogonal approach, we performed GSEA on genes differentially expressed in H3B-8800-treated compared to vehicle-treated tumors. Hierarchical clustering of pathways commonly enriched amongst models revealed a pronounced cluster comprised almost exclusively of antiviral and adaptive immune pathways enriched solely in sensitive tumor models (Figure 6D and Table S3). These findings provide evidence that STTs activate not only tumor antiviral signaling but also adaptive immune signaling in models sensitive to this single agent regimen. Furthermore, these pathways are negatively enriched in resistant tumor models, supporting the hypothesis that activation of antiviral immune signaling is crucial for the antitumor activity of STTs.

The observation that H3B-8800 induced strong antiviral transcriptional patterns specifically in sensitive tumor models supports the hypothesis that the STT-induced dsRNA-antiviral response observed in human TNBC models (Figures 1–5) also occurs in these sensitive murine TNBC cells. To confirm that gene expression changes in non-tumor cells did not confound our analysis, we derived *in vitro* cell lines from these syngeneic models to investigate the tumor cell-intrinsic response to STT. While H3B-8800 induced IR across all models *in vitro*, H3B-8800 induced more IR in the 2208L and PyMT-M cell lines (from

sensitive tumor models) than in AT3 and T11 cell lines (from resistant tumor models) (Figure S6C), consistent with results from bulk tumors *in vivo*. Additionally, H3B-8800 treatment induced significantly greater accumulation of dsRNA in 2208L and PyMT-M cell lines than in AT3 and T11 cell lines (Figure 6E). Importantly, H3B-8800 induced antiviral transcriptional targets *Cxcl10*, *Cxcl11*, *Tlr9* (Figure 6F) and secretion of CXCL10 protein (Figure S6D) in sensitive cell lines but had little or no effect in resistant cell lines (Figure 6F), suggesting that intron retention and dsRNA accumulation correlate with downstream induction of antiviral pathways in murine TNBC cells. Notably, cell lines from resistant tumor models (AT3 and T11) were largely recalcitrant to H3B-8800-induced cell death (Figure S6E). In contrast, H3B-8800 strongly induced apoptosis in tumor cells from the 2208L tumor model, consistent with its strong activation of dsRNA-antiviral programs and sensitivity to H3B-8800 *in vivo* (Figure S6E). Interestingly, H3B-8800 did not induce caspase-8 in tumor cells from the PyMT-M tumor model despite a strong activation of dsRNA antiviral response, possibly due to suppression of caspase-8 activity by the PyMT viral oncoprotein (Courtneidge and Smith, 1983; Tsang et al., 2016). Consistent with this observation, prior reports indicate that induction of antiviral transcriptional programs and apoptotic (caspase-8) mechanisms downstream of dsRNA sensing can be independent (Lei et al., 2009), and that these two outputs may be disengaged in some contexts. These results raise the possibility that H3B-8800-mediated tumor control in the PyMT-M model (and perhaps other tumor contexts) may occur through tumor cell non-autonomous mechanisms, a hypothesis that requires further investigation. Together, these data further support the model that accumulation of mis-spliced and double-stranded RNA induces antiviral signaling pathways within tumor cells.

Our RNA-seq analysis indicated that in addition to antiviral signaling, signatures associated with adaptive immune engagement were upregulated in sensitive syngeneic models. H3B-8800 treatment led to increased expression of several T cell chemoattractants (such as *Cxcl9* and *Cxcl10*) and corresponding adaptive immune gene sets (Figures 6C and 6D). On closer examination, expression of *Cd4* and multiple common markers of T cell activation were increased in sensitive (but not resistant) models with H3B-8800 treatment (Figures S6F–S6I), which supports potential engagement of host T cells. We also assessed the “cytolytic index”, the co-expression of both granzyme A (*Gzma*) and perforin (*Prf1*), as a proxy for CD8+ T cell activity (Rooney *et al.*, 2015). Notably, the cytolytic index was increased following H3B-8800 selectively in sensitive models (Figure S6J), suggesting CD8+ T cell activation in response to treatment with H3B-8800. Indeed, tumor infiltration of CD8+ T cells was significantly increased upon H3B-8800 treatment in PyMT-M tumors (Figures S6K and S6L), consistent with upregulation of gene sets related to T cell co-stimulation and T cell receptor signaling (Figure 6D). Overall, these findings support the model that spliceosome inhibition induces upregulation of both antiviral and adaptive immune signaling in tumor cells, and provoke the hypothesis that STTs may, in some contexts, stimulate anti-tumor immunity, an area of study that requires further investigation.

Defects in RNA Splicing and MYC Amplification Correlate with Immune Response in Human Breast Cancer

The observations that global defects in tumor RNA splicing may activate adaptive immune signaling in murine models of breast cancer raise the question of whether similar effects occur in human breast cancer. While the effects of STTs have not yet been evaluated in breast cancer patients, we hypothesized that tumors with intrinsic global defects in splicing (as indicated by widespread IR) may instigate an immune response. To evaluate this hypothesis, we computed global IR levels across 983 TCGA primary breast tumors (Koboldt et al., 2012) and tested whether elevated IR correlates with expression signatures of tumor infiltrating immune cells using immune cell single sample GSEA analysis (Barbie *et al.*, 2009). Remarkably, tumor IR levels significantly correlated with previously characterized T cell immune infiltration signatures (Bindea *et al.*, 2013), including helper, memory, and effector T cells (Figure 7A and Table S4). When IR was considered as a categorical variable (high being >1 SD above and low being >1 SD below the cohort mean), IR continued to associate significantly with the same signatures (Figure 7A). We then used GSEA to more broadly query gene expression differences between tumors with high and low intrinsic IR. Notably, immune signaling-related pathways made up 36% of significantly positively enriched pathways (FDR ≤ 0.01) (Figure 7B). Tumor mutational burden (TMB), a feature of cancers previously shown to be associated with immune recruitment and anti-tumor immunity (Rizvi et al., 2015; Snyder et al., 2014), was negatively correlated with IR levels in this cohort (Figure S7A), suggesting tumor-intrinsic IR is a distinct feature correlating with immune engagement. Importantly, high IR is associated with improved patient disease-free survival (Figure 7C), suggesting that improved tumor control may be, in part, due to increased immune engagement seen in tumors with high levels of RNA mis-splicing.

MYC has been demonstrated to suppress immune engagement (Bernards et al., 1986; Casey et al., 2018, 2017, 2016; Kortlever et al., 2017; Topper et al., 2017) and drive poor prognosis breast cancers (Al-Kuraya et al., 2004; Aulmann et al., 2006; Deming et al., 2000; Robanus-Maandag et al., 2003; Schlotter et al., 2003). However, this study has uncovered that oncogenic MYC primes cancer cells to activate antiviral immune signaling in the context of spliceosome perturbation. Therefore, we hypothesized that MYC amplification in tumor cells might augment the immune signaling associated with high baseline RNA mis-splicing. To test this, we divided tumors into four cohorts based on MYC copy number (amplified or normal as measured by GISTIC) and intron retention (IR high or low using aforementioned cutoffs). Utilizing GSEA, we compared gene expression patterns of tumors in each of these cohorts to determine enrichment profiles unique to each group. Importantly, 7 of the top 10 enriched pathways in the high IR high MYC cohort were related to immune signaling (Figure 7D), while high IR normal MYC cohort exhibited enrichment of only 1 immune pathway. This same pattern was not observed with CCNE1, another commonly amplified gene in breast cancer (Figure 7E), suggesting a unique interaction between MYC and IR to induce immune signaling. These data are concordant with previous work (Hsu et al., 2015) demonstrating that MYC drives sensitivity to spliceosome inhibition. More broadly, this lends evidence to the idea that IR burden may be a quantifiable intrinsic feature of tumors, and that IR burden above a threshold could promote immune signaling in certain oncogenic contexts (like MYC amplification). The strong correlation of defective RNA processing

and T cell recruitment could arise through multiple non-mutually exclusive mechanisms like activation of antiviral signaling and consequent recruitment of T cells, expression of neo-antigens, or others yet to be elucidated. Nonetheless, these data provoke the hypothesis that global RNA splicing defects, whether tumor intrinsic or induced by acute spliceosome inhibition, may stimulate adaptive immune responses.

DISCUSSION

Small molecule modulators of the spliceosome exhibit potent anti-tumor activity across many cancers, though the mechanisms by which they kill tumors have been unclear. Important studies have characterized the mis-splicing of single genes or gene families in response to spliceosome inhibition, leading the field to focus on these aberrant protein products to explain sensitivity to spliceosome therapeutics. In contrast, we find that mis-spliced RNA itself may have an unrealized, broader function as a macromolecule in dictating tumor cell sensitivity to spliceosome inhibition. Our results show that tumor cell death is associated with accumulation and recognition of intron-resident dsRNA and subsequent activation of antiviral immune pathways. These results highlight endogenous mis-spliced RNA as an unexpected substrate for dsRNA sensors that can be leveraged therapeutically to engage a tumor cell-intrinsic immune response. Activation of tumor-intrinsic immune signaling via dsRNA-recognition pathways has been studied recently in the context of DNA methyltransferase inhibitors (Chiappinelli et al., 2015; Luo et al., 2018; Roulois et al., 2015; Stone et al., 2017) and *ADAR* perturbations (Gannon et al., 2018; Ishizuka et al., 2019; Liu et al., 2018). However, in these scenarios it is unclear whether there is selectivity in dsRNA induction across tumor types or between tumor and non-malignant tissues. This study identifies introns as a distinctive source of endogenous dsRNA substrates that can be differentially induced in cancer cells, particularly those with hyperactivation of the MYC oncogene.

As recent clinical trials have demonstrated profound albeit heterogeneous success in modulating the immune system to treat cancer (Sharma et al., 2017), the community has searched for tumor-intrinsic features that dictate whether the immune system can be stimulated to recognize and eliminate cancer cells. For instance, tumor mutational burden (TMB) and high burden of clonal tumor neoantigens have been shown to drive T cell infiltration into the tumor (McGranahan et al., 2016) and these features strongly associate with success of immune-checkpoint blockade (Cristescu et al., 2018; Goodman et al., 2017; Hugo et al., 2016; Rizvi et al., 2015; Yarchoan et al., 2017). However, DNA aberrations (e.g. somatic mutations) are likely only one among many characteristics of tumors that drive tumor recognition by the immune system. We provide evidence that a high burden of RNA mis-splicing (in the form of intron retention) may be an unexplored feature of some cancers that engages tumor antiviral signaling and downstream adaptive immunity. Indeed, analysis of primary breast cancers supports this hypothesis, with tumors that harbor high levels of intron retention also exhibiting overexpression of gene expression programs enriched for immune pathways, especially in tumors with MYC amplification. This observation suggests that inherent RNA processing defects, which are a pervasive but heterogeneous feature of cancers, may induce tumor-intrinsic immune signaling in some contexts. It

also raises the therapeutic hypothesis that RNA splicing defects may prime sensitivity to immune-checkpoint blockade or other therapies that engage adaptive immunity.

Finally, our results engender the idea that activation of cell-intrinsic antiviral immunity may be a common mechanism that responds to widespread splicing defects across cancer and other disease states. Aberrations in macromolecules such as DNA and protein are recognized by well-established pathways, such as the DNA damage response (DDR) and unfolded protein response (UPR). These pathways regulate coordinated responses to these aberrations to either restore cellular homeostasis or cause cell death, and in some contexts, serve as potent oncogenic checkpoints to prevent tumorigenesis. In contrast, while we are aware of important quality control mechanisms for RNA such as nonsense-mediated decay, it has been unclear whether there are signaling pathways that sense widespread mis-splicing of RNA and dictate cell fate (e.g. apoptosis). We provide evidence that dsRNA sensing and antiviral signaling may serve as such a coordinated response for widespread mis-splicing of RNA, with intron-resident dsRNAs serving as a trigger for this response. Our data support the involvement of multiple dsRNA sensors, including but not limited to those that interface with MAVS, in dictating cell fate in response to widespread RNA mis-splicing. Our data suggest the presence of diverse pools of intron-containing dsRNA and concordant dsRNA sensors that trigger this antiviral immune response. In the future, it will be important to elucidate which pools of endogenous dsRNAs stimulate dsRNA-sensors, and how the varied genetic/epigenetic context of cancer drivers like MYC may influence these dsRNA pools and sensors and prime tumors to dsRNA antiviral immune responses. More broadly, aberrantly spliced transcripts may be similarly sensed as dsRNA triggers in other pathologies with well characterized RNA processing defects such as Alzheimer's disease, which is characterized by broad accumulation of mis-spliced RNA (Bai et al., 2013; Raj et al., 2018; Vaquero-Garcia et al., 2016; Wyss-Coray, 2006). This raises the exciting possibility that antiviral immune signaling, a critical component of Alzheimer's disease pathogenesis, may be activated by surveillance and sensing of aberrantly spliced RNAs. Overall, our findings reveal dsRNA-mediated antiviral immunity as a sensing and response mechanism for broad cellular splicing defects, suggesting that deregulated RNA processing may contribute to cellular antiviral pathway activation in cancer and other diseases.

LIMITATIONS AND FUTURE DIRECTIONS

This study has focused on exploring the tumor cell-intrinsic responses to STTs, revealing that spliceosome inhibition triggers accumulation of dsRNA and activation of antiviral signaling pathways. Moreover, acute therapeutic spliceosome inhibition is sufficient in some contexts to stimulate both antiviral and adaptive immune signaling, as well as tumor T cell infiltration. However, further studies are needed to investigate the contribution of the adaptive immune response to the anti-tumoral activity of STTs. There are several outstanding questions requiring investigation. How does tumor-cell intrinsic activation of antiviral pathways in the context of STT treatment or other scenarios of RNA misprocessing communicate to the host adaptive immune compartment? What compartments of the adaptive immune system, if any, are required for STT anti-cancer efficacy? What are the effects of STTs on immune cell types and do they elicit counter-balancing effects on anti-tumor immunity? These areas of exploration will be critical to exploring whether STTs

can be leveraged to galvanize the immune system against aggressive, immune-cold tumors like TNBC.

STAR Methods

RESOURCE AVAILABILITY

Lead Contact—Further information and requests for resources and reagents should be directed to and will be fulfilled by the Lead Contact, Thomas Westbrook (thomasw@bcm.edu).

Materials Availability—All unique/stable reagents generated in this study are available from the Lead Contact with a completed Materials Transfer Agreement.

Data and Code Availability—The datasets generated during this study are available in GEO [GSE163411, GSE163414, GSE163181, GSE163188, GSE163232].

EXPERIMENTAL MODEL AND SUBJECT DETAILS

For cell line studies, SUM159 (female) cells were cultured in F12 media supplemented with 5% FBS, 10mM HEPES, 5ug/mL insulin, and 1ug/mL hydrocortisone. MDA-MB-231 (female), MDA-MB-231-LM2 (female) (Minn et al., 2005), and 293T cells were cultured in DMEM media supplemented with 10% FBS. BT549 cells were cultured in RPMI 1640 media supplemented with 10% FBS. HME1 (female) cells were cultured in MEGM (Lonza, CC-3150). MYC-ER HME1 cells were cultured in MEGM and treated with 10uM 4-hydroxytamoxifen (4-OHT) where indicated to induce MYC hyperactivation. PyMT-M (female), 2208L (female), and AT3 (female) cells were cultured in DMEM media supplemented with 10% FBS and 1% Penicillin Streptomycin. T11 (female) cells were cultured in DMEM/F12 media supplemented with 10% FBS, 5ug/mL insulin, 1ug/mL hydrocortisone, 10ng/mL EGF, and 1% Penicillin Streptomycin. These cell lines were routinely tested for Mycoplasma contamination in the laboratory. All cell lines were incubated at 37°C and 5% CO_2.

For in vivo animal studies, all animal protocols related to mouse experiments were approved by the Baylor College of Medicine Institutional Animal Care and Use Committee (protocol AN-6672). 4–5-week-old female C57BL/6J and BALB/c AnNHsd mice were obtained from The Jackson Laboratory (000664) and Envigo (4701F), respectively. Mice were housed in ventilated cages in a pathogen-free animal facility under a 14hr light/10hr dark cycle. 2208L, PyMT-M, and AT3 tumors were randomized onto vehicle or H3B-8800 at 150–250mm^3 for long term response studies or 300–500mm^3 for short term studies. Animals were allocated into treatment groups so that the average tumor size in both groups was similar. T11 tumors were randomized onto vehicle or H3B-8800 one day post tumor transplant. Sample size was determined for each syngeneic model separately based on previous tumor kinetic data.

METHOD DETAILS

Cell culture—Stable cell lines expressing shRNAs, sgRNAs, or cDNA were generated by retroviral or lentiviral transduction using 8ug/mL polybrene. Cells were selected using

puromycin (1ug/mL). Transient depletion of genes using siRNA was achieved by reverse transfection of cell with 10pmol siRNA in RNAiMax for 12 hours. Depletion of target genes using shRNA or siRNA was confirmed using RT-qPCR. Knockout of genes using sgRNAs or expression of exogenous cDNA was confirmed using Western blotting. See Table S5 for sequences of shRNAs used. See Table S5 for sequences of siRNAs used. See Key Resources Table for sgRNAs used.

Vectors and virus production—Lentiviruses and retroviruses were generated by transfection of 293Ts with appropriate shRNA, sgRNA, or cDNA construct with packaging plasmids using Mirus Bio's TransitIT transfection reagent. Viral supernatants were harvested 48 hours after transfection.

RNA isolation and library preparation—Total RNA (1ug/sample) was used as input for the TruSeq Stranded mRNA HT Prep Kit (Illumina). Libraries were made following Illumina's recommended protocol, except for dsRNA libraries. For library preparation of J2 enriched dsRNA, first stranded cDNA synthesis was performed using SuperScript III (ThermoFisher Scientific) with the following modifications: RNA was heated to 70°C for 3 minutes to reduce secondary structure, followed by reverse transcription for 10 minutes at 25°C, 50 minutes at 50°C, and 15 minutes at 70°C. Amplified libraries were purified and quantified using the KAPA quantification kit (Roche). Libraries were sequenced on the Illumina NextSeq 500 instrument as 75-bp paired-end reads. In Figures 1A–1D SD6 gene expression analyses, cells were treated with DMSO or SD6 GI40 dose (200nM for SUM159 and 50nM for LM2).

Alignment of sequencing data—After demultiplexing, reads for both human and mouse samples were processed using SAMtools (v1.4) (Li et al., 2009) and aligned using the splice aware aligner Hisat2 (v2.0.4) (Kim, Langmead and Salzberg, 2015) with default parameters. The coordinates and gene annotations used in all subsequent analyses were based on the human (hg38/GRCh38) and mouse (mm10/GRCm38) reference genome builds and the corresponding UCSC RefSeq genes unless otherwise noted.

Gene expression and retrotransposon expression analysis—Gene expression FPKM values used for downstream GSEA analyses were obtained using the cufflinks suite (v2.2.1) (Trapnell *et al.*, 2010). For analysis of differential gene expression changes in "sensitive" vs. "resistant" syngeneic tumors after H3B-8800 treatment, the following pipeline was employed: featureCounts (v1.6.2) (Liao, Smyth and Shi, 2014) was used to quantify counts, followed by interaction analysis using DESeq2 (Love, Huber and Anders, 2014) with the following design: ~ response + treatment + response:treatment. Annotations for repeat elements were obtained from RepeatMasker (open-4.0.5). Counting of reads mapped to annotated repeat elements was performed using the Python module Pysam (Li et al., 2009). Expression was then RPKM normalized.

Pathway enrichment analysis—Gene set enrichment analysis (GSEA) was performed on genes differentially expressed after spliceosome inhibition in human cell lines and syngeneic murine tumors ($p \geq 0.05$). Reactome pathways from the MSigDB database (Liberzon et al., 2011; Subramanian et al., 2005) were used for human data analysis; the

"Mouse_AllPathways_June_24_2016_symbol.gmt" pathway collection from the Bader lab (http://baderlab.org/GeneSets), consisting of C2 Canonical Pathways (C2 CP) was used for mouse GSEA data analysis. Pathway over-representation of genes with differential gene expression changes in "sensitive" vs. "resistant" syngeneic tumors after H3B-8800 treatment was performed using Metascape (Zhou et al., 2019) using C2 CP annotations.

Intron retention (IR) analysis—Hisat2-aligned reads were filtered for proper-paired reads (-f 2 flag in SAMtools). Intron annotations were parsed from UCSC RefSeq gene annotation files and were filtered to exclude features that overlap genomic loci on the same strand. Reads mapping to introns were counted using Pysam. For each intron feature, we defined the following two read classes: (1) "intronic" reads mapping at least 6 bases contiguously within the intron and (2) "spanning" reads with ends mapping to the flanking exons. The intron retention (IR) score was then computed as the ratio of the RPKM-normalized "intronic" read density over the RPKM-normalized "spanning" read density. In order to compare commonly expressed IR events across samples, introns with <10 spanning RPKM in any sample were excluded from all analyses. Statistical analyses were performed using R. Empirical cumulative distributions of IR scores were compared, and p-values estimated using a Mann-Whitney *U* test.

Quantitative reverse transcription PCR (RT-qPCR)—Total RNA was isolated using the RNeasy Mini Kit (Qiagen). Synthesis of cDNA was done using the High-Capacity RNA-to-cDNA Kit (Applied Biosystems). RT-qPCR was performed using the SYBR Select Master Mix (Applied Biosystems) on 20ng of input cDNA. Relative transcript abundance was normalized (*GAPDH* for human samples, *18s* for mouse samples) and assessed using the Applied Biosystems StepOne Software v2.1. Data were calculated as $\log_2$(fold change) relative to control data using the ΔΔCt method. All experiments were performed in biological triplicate. For intron retention analysis, primer sets were designed to measure intron-containing transcripts and fully spliced transcripts. Intron retention was calculated as the ratio of intron-containing transcripts over fully spliced transcripts. Data were calculated as fold change relative to control data using the ΔΔCt method. For enzymatic dsRNA structure probing, relative transcript abundance was normalized (*ACTB*) and data were calculated as fold change relative to control data using the ΔΔCt method. In Figure 1G–H, MYC-ER HME1 cells were treated with 10nM 4-OHT and 10nM H3B-8800. In Figure 2E, SUM159 cells were treated with 200nM SD6. In Figures 5J and S5W, SUM159 cells were treated 15nM H3B-8800. In Figure 4, SUM159 cells were treated with 100nM H3B-8800. In Figure S5F, SUM159 cells were treated with 100nM H3B-8800. In Figure 6I, syngeneic tumor-derived cell lines were treated with 50nM H3B-8800. In Figure 6K, syngeneic tumor-derived cell lines were treated with 25nM H3B-8800. See Table S6 for primer sequences.

RT^2 Profiler PCR Array—Innate immune transcriptional changes in response to treatment with H3B-8800 were measured using RT^2 Profiler PCR Array Human Antiviral Response (Qiagen, 330231) following treatment of SUM159s (DMSO or 25nM H3B-8800) and LM2s (DMSO or 25nM H3B-8800). Relative transcript abundance was normalized to *B2M* and assessed using the Applied Biosystems StepOne Software v2.1. Data were calculated as fold

change relative to control data using the ΔΔCt method. All experiments were performed in biological triplicate.

Luminex Cytokine Analysis—SUM159 cells were treated with DMSO or 25nM H3B-8800 and conditioned media was collected for analysis using the Luminex Assay. Conditioned media was incubated overnight with analyte targeted beads and analyte concentration was calculated based on analyte standard curve. Concentration was normalized to cell number determined by Hoechst 33342 (Life Technologies) staining of a duplicate plate, followed by nuclei counting using the Celigo Imaging Cell Cytometer (Brooks).

SUM159 SF3B1- FKBP12^{F36V} cell line generation and assays—The FKBP12^{F36V} fragment (Nabet *et al.*, 2018) was fused to the C-terminus of *SF3B1* cDNA and cloned into a pHAGE-PGK backbone. Cas9 was amplified from pCW-Cas9 (Wang et al., 2014) and cloned into pINDUCER20 to allow for dox-inducible Cas9 expression (Meerbrey *et al.*, 2011). This vector was transduced into SUM159 cells and was selected with neomycin. A clone was selected to generate SUM159-Cas9 cells with homogenous Cas9 expression and inducibility. SUM159 cells stably expressing dox-inducible Cas9 were transduced with the SF3B1-FKBP12^{F36V} lentivirus and then selected with puromycin. To knock out the endogenous *SF3B1* locus, Cas9 expression was turned on with 500 ng/mL of doxycycline for 24 hours, followed by 48 hour co-transfection of Edit-R tracrRNA (Dharmacon) and crRNA targeting the first intron-exon junction of SF3B1. A single clone was then selected, and Western blotting was used to confirm knockout of the endogenous protein and expression of SF3B1- FKBP12^{F36V}. SF3B1 degradation was assayed using 10nM dTAG-51 (Nabet *et al.*, 2018) for the stated durations. Gene expression analysis in Figure 1J was performed following treatment with DMSO or 10nM dTAG-51. Immunofluorescence assay in Figure 3F were performed following 10nM dTAG-51 treatment.

Western blot—Cell lysates were collected in RIPA Buffer + Protease Inhibitor Cocktail (Roche, 11836170001) + Phosphatase Inhibitor Cocktail 2 (Sigma, P5726), then mixed with 6× Laemmli SDS reducing buffer (Alfa Aesar, J61337) before incubation at 95°C for 10 minutes. Protein lysates were quantified using Pierce BCA Protein Assay (Thermo Scientific, 23225). Samples were loaded for SDS-PAGE using homemade tris-glycine gels and run in SDS running buffer.

Proteins were transferred using wet transfer to 0.45μM Nitrocellulose membrane (GE Healthcare Life Science, 10600007). The membrane was blocked for 1 hours using 5% BSA in TBS-T (0.1% Tween-20 in 1× TBS) and incubated with primary antibody overnight at 4°C. The membrane was then washed 3 times in TBS-T for 5 minutes before incubation with the secondary antibody at RT for 2 hours. The membrane was then washed 3 times with TBST before incubation with Clarity Western ECL Substrate (Bio-Rad, 170–5060) and imaging with the ChemiDoc MP Imaging System (Bio-Rad).

shRNA screen—SUM159s were transduced with a MSCV-based retroviral library (Rousseaux et al., 2018) containing a total of 18,370 shRNAs divided into two separate pools at a MOI of 0.5 and a target representation of 1000 cellular integrations for each

shRNA. After transduction, cells were selected for 3 days in puromycin, then split into parallel +/− SD6 arms (in quadruplicate) and cultured for 12 population doublings. During this time, cells were passaged every 3 days (6 passages for DMSO treated, 7 passages for SD6 treated). After selection (T0) and at each subsequent passage, 20 million cells were collected from each replicate and stored at −80°C. Cell pellets from T0 and the final passage were used for downstream analysis.

Library preparation and sequencing—The QIAamp DNA Blood Midi kit (QIAGEN) was used to extract genomic DNA from cell pellets followed by ethanol precipitation to clean and concentrate. Half-hairpin sequences were amplified from the genomic DNA (primers 5'-TCGTCGGCAGCGTCAGATGTGTATAAGAGACAGTAGTGAAGCCACAGATGTA-3' and 5'-GTCTCGTGGGCTCGGAGATGTGTATAAGAGACAGTATAAACGGTTGGTCTTCCAA-3') using Q5 High-Fidelity 2X Master Mix (NEB). PCR reactions were cleaned up using Agencourt AMPure XP beads (Beckman Coulter) followed by measurement of the concentration of the target amplicon using the Agilent 4200 TapeStation. DNA samples were indexed using the Nextera XT kit (Illumina) and size selected to remove spurious amplification products using the PippinHT (Sage Science). Indexed and size-selected samples were quantified using the KAPA Illumina Library Quantification kit (KAPA Biosystems) and pooled at equal concentration prior to sequencing using the HiSeq 2500 System (Illumina) in single-end, 100bp, high-output mode using v4 SBS reagents.

Data processing and analysis—Cutadapt (Martin, 2011) was used to remove adapter sequences from reads, followed by alignment to the reference library using Bowtie 2 (Langmead and Salzberg, 2012) in end-to-end mode, allowing up to a maximum of 3 mismatches/indels compared to the reference sequence. The number of reads mapping to each shRNA in each sample was then extracted from the SAM files and DESeq2 (Love, Huber and Anders, 2014) was used to determine the fold-change in abundance of each shRNA between the vehicle and SD6-treated arms after 12 population doublings. shRNA-level fold-change estimates were combined to gene-level estimates by summing the individual fold-changes of all "significant" shRNAs (p-value <0.05 and absolute fold-change > 0.5) mapped to a given gene. Gene-level p-values were calculated by combining the individual p-values of all "significant" shRNAs mapping to a given gene using Fisher's method. Gene-level weighted growth effects were calculated by multiplying the gene-level fold change by the $-\log_{10}$ (gene-level p-value).

Screen candidate MeSH and StringDB analysis—Analysis of over-represented Medical Subject Headings (MeSH) was performed using the R package "meshes" (v1.8.0) (Yu, 2018) with the following parameters: MeSHDb = 'MeSH.Hsa.eg.db', database = 'gene2pubmed' and category = 'C'. For Cytoscape visualization, individual genes in MeSH term categories were set as nodes and common MeSH terms as edges. Pathway over-representation for screen candidates was performed using StringDB (v11.0) (Szklarczyk et al., 2019).

Competition assays—SUM159 cells were transduced with MSCV retroviral shRNAs targeting Firefly luciferase (shControl), RNF128, RNF125, UBE2D1, or USP1 and selected for three days with puromycin. After selection, these cells were mixed at a 40:60 ratio with SUM159 cells transduced with pHAGE-PGK-E2 Crimson and grown in 96-well plates in the presence of DMSO or 200nM SD6. At seeding and when the cells reached confluence, cells were passaged and the percentage of E2-Crimson-positive cells was measured by flow cytometry. The percentage of shRNA knockdown cells was calculated as the percentage of non-E2 Crimson positive cells.

Fluorescent immunohistochemistry—Cells were washed with PBS, fixed with 4% (v/v) formaldehyde for 15 minutes at room temperature, washed 3 × with PBS, and permeabilized with 0.5% (v/v) Triton-X for 10 minutes at RT. Cells were blocked with 3% BSA in PBS for 15 minutes at RT before incubating with primary antibody (monoclonal anti-dsRNA J2 (Scicons, 10010500) (Schönborn *et al.*, 1991), monoclonal anti-MAVS (Cell Signaling, 24930)) diluted in blocking buffer at 4°C overnight. Cells were washed 3 × with PBS before incubation with secondary antibody (Alexa Fluor 488 goat anti-mouse IgG (Invitrogen, A11029) for J2 antibody and Alexa Fluor 594 goat anti-rabbit IgG (Invitrogen, A11012) for MAVS antibody), Hoechst 33342 (Invitrogen, H3570), and Phalloidin (Invitrogen, A12381) for 1 hour at RT in the dark. Cells were washed 3 × with PBS before mounting on coverslips with Vectashield (Vector Laboratories, H-1000).

J2 immunofluorescence imaging and analysis—SUM159, MDA-MB-231, and BT549 cells were treated with DMSO or 100nM H3B-8800 before processing. LM2 cells were treated with DMSO or 50nM H3B- before processing. In Figure 3E, MYC-ER HME1 cells were treated with 10nM 4-OHT and 20nM H3B-8800. In Figure S3C, SUM159 and HME1 cells were treated with DMSO or 50nM H3B-8800 before processing. In Figure 6J, syngeneic tumor-derived cell lines were treated with DMSO or 20nM H3B-8800 before processing. When indicated, cells were incubated with 4U RNaseIII (Applied Biosystems, A2290) in reaction buffer at 37C for 4 hours as instructed after permeabilization. For J2 dsRNA imaging, cells were imaged and analyzed on a Nikon Eclipse Ti-E inverted microscope with the NIS-Element AR 4.30 software. Briefly, images were captured with Z-stacked (0.3um) setting under 60X oil objective lens and Andor Zyla 4.2 sCMOS camera. For quantification the cytoplasmic J2 intensity, a ROI defining cytoplasm was determined by the Hoechst and Phalloidin staining for each cell. The average fluorescent intensity for defined ROIs and background from the same image were directly measured by the NIS-Element AR software. J2 intensity for each cell was defined by difference between the ROI and background intensity. J2 intensity was normalized to mean intensity in the DMSO treated state for each experiment. Plots shown in figures are from one representative experiment of more than three independent experiments.

SF3B1^{R1074H} cell line generation and assays—The SF3B1^{R1074H} mutant was generated in pDONR221 using the QuikChange II Site Directed Mutagenesis Kit (Agilent). SF3B1^{WT} and SF3B1^{R1074H} were FLAG-tagged then cloned into pINDUCER20 to allow for dox-inducible expression. This vector was transduced into SUM159 and LM2 cells. H3B-8800 dose curve assay was performed by treating SUM159 and LM2 cells with

1ug/mL doxycycline followed by the indicated concentration of H3B-8800. Cell numbers were determined by Hoechst 33342 staining, followed by nuclei counting using the Celigo Imaging Cell Cytometer (Brooks). Western blot analysis of inducible protein expression was performed with the same treatment conditions. Intron retention following treatment of SUM159 cells ± 1 ug/mL doxycycline for 24 hours followed by 12 hours of treatment with 100nM H3B-8800 using RT-qPCR. Immunofluorescence assays were performed ± 1 ug/mL doxycycline for 24 hours followed by DMSO or 50nM H3B-8800 treatment.

Cellular fractionation—SUM159 cells were treated with 100nM H3B-8800 or DMSO, collected in biological duplicate in ice-cold PBS, then spun down at 180g for 5 minutes at 4°C. Supernatant was removed, and cells were lysed in cytoplasmic lysis buffer (CLB: 10mM HEPES, pH 7.9, 10mM KCl, 1mM MgCl2, 0.5mM EDTA, 1mM DDT, 0.1% Igepal CA-630, 1 U/ul RNasin Plus) for 5 minutes on ice. Lysates were spun down at 1000g for 5 minutes at 4°C. The supernatant, or cytoplasmic fraction, was transferred to separate tubes for collecting RNA and protein. The cell pellet was washed once with CLB and lysed on ice in high salt nuclear lysis buffer (50 mM Tris-Cl, pH 7.4, 300 mM NaCl, 1mM MgCl2, 0.5% Igepal CA-630, 0.1% SDS) for 5 minutes on ice. The lysate was then divided for collecting RNA and protein. Equal cell-normalized quantities of protein were analyzed by Western blot to confirm fractional purity (total H3 for nuclear fraction, α-Tubulin for cytoplasmic fraction).

RNA fluorescent in situ hybridization—Custom Stellaris® FISH probes were designed against *SEC14L1* and *SETD1A* by utilizing the Stellaris® RNA FISH Probe Designer (Biosearch Technologies, Inc., Petaluma, CA) available online at www.biosearchtech.com/stellarisdesigner (see Table S8 for probe sequences). The probe sets were hybridized with TAMRA (intronic probe sets) and Quasar 670® (exonic probe sets). RNA FISH was performed following the manufacturer's instructions available online at www.biosearchtech.com/stellarisprotocols. with minor modifications. In brief, SUM159 cells were treated with DMSO or 100nM H3B-8800. Fixation and permeabilization were performed as described for immunofluorescence. After permeabilization, cells were washed 2 × with PBS and 1× with Wash Buffer A (Bioresearch Technologies, SMF-WA1–60) with 10% (v/v) formamide (Ambion, AM9342) at RT for 5 minutes. Coverslips were than incubated in the Hybridization Buffer (Bioresearch Technologies, #SMF-HB1–10) with 10% (v/v) formamide containing indicated probes at 37°C overnight in a humidified chamber. Coverslips were washed with Wash Buffer A at 37°C for 30 minutes, then incubated with Wash Buffer A containing Hoechst for 37°C for 30 minutes. Samples were then washed with Wash Buffer B (Bioresearch Technologies, #SMF-WB1–20) at RT for 5 minutes. Coverslips were mounted onto microscope slides with Vectashield (Vector Laboratories, H-1000). All steps following hybridization were done protected from light. Imaging was performed and processed as previously described using a GE Healthcare DVLive epifluorescence microscope. After imaging, Z-stacks were transformed into a 2D image by maximal projection. Cytoplasmic intron and exon foci for each cell were manually counted by the ImageJ software. Plots shown in figures are representative of two independent experiments.

dsRNA immunoprecipitation (J2 dsRIP)—Protein A Dynabeads were washed and resuspended in NT-2 buffer (50 mM Tris-Cl, pH 7.4, 150 mM NaCl, 1 mM MgCl2, 0.1% Igepal CA-630). Per sample, 100ul of beads were pre-bound to 5 ug of anti-dsRNA mAb (J2) overnight at 4°C. SUM159 cells were treated with 100nM H3B-8800 or DMSO, collected in biological duplicate in ice-cold PBS, then spun down at 180g for 5 minutes at 4°C. Supernatant was removed, and cells were lysed in 1mL RIP buffer (25 mM HEPES pH 7.2, 150 mM NaCl, 5 mM MgCl2, 0.1% Igepal CA-630, 1 U/ul RNasin Plus) for 5 minutes on ice. The supernatant was transferred to a new Eppendorf. Total RNA was harvested from 10% input lysate using Trizol. For immunoprecipitation, 100 ul of J2-bound Protein A Dynabeads was added to the remaining lysate and incubated for 3 hours at 4°C with constant mixing. Beads were washed three times with NT-2 buffer, transferred to a new tube, and then washed three times with high salt wash buffer (50 mM Tris-Cl, pH 7.4, 300 mM NaCl, 1mM MgCl2, 0.5% Igepal CA-630, 0.1% SDS). J2-bound dsRNA was harvested directly from beads with Trizol. Chloroform was added at a ratio of 1:5, and RNA was isolated from the aqueous phase using the RNA Clean and Concentrator columns (Zymo).

RNA structure prediction—RNA structure prediction was done using the RNAfold web server (http://rna.tbi.univie.ac.at/cgi-bin/RNAWebSuite/RNAfold.cgi) with default options.

Enzymatic dsRNA structure probing—SUM159 cells were treated with 100nM H3B-8800 or DMSO, collected in biological triplicate in ice-cold PBS, then spun down at 180g for 5 minutes at 4°C. Supernatant was removed and cells were snap frozen in liquid nitrogen. Cells were lysed in 1mL RIP buffer (25 mM HEPES pH 7.2, 150 mM NaCl, 5 mM MgCl2, 0.1% Igepal CA-630, 1 U/ul RNasin Plus) for 5 minutes on ice. The supernatant was transferred to a new Eppendorf. Lysates were treated with or without 5U RNaseOne (Promega, M4261) for 30 minutes at room temperature. RNA was harvested using Trizol. Chloroform was added at a ratio of 1:5, and RNA was isolated from the aqueous phase using the RNA Clean and Concentrator columns (Zymo). First stranded cDNA synthesis was performed using SuperScript III (ThermoFisher Scientific) with the following modifications: RNA was heated to 70°C for 3 minutes to reduce secondary structure, followed by reverse transcription for 10 minutes at 25°C, 50 minutes at 50°C, and 15 minutes at 70°C. Transcript abundance was measured using RT-qPCR using the SYBR Green Master Mix (Applied Biosystems) on 20ng of input cDNA. Relative transcript abundance in samples treated with and without RNaseOne was normalized (*ACTB*) and assessed using the Applied Biosystems StepOne Software v2.1. The dsRNA/ssRNA fold enrichment was calculated using the ΔΔCt method comparing relative transcript abundance in the sample treated with RNaseOne to the sample treated without RNaseOne.

Cell viability assays—PI positive cells were assessed by incubating cells with 1:100 dilution of Propidium Iodide (Sigma Aldrich, P4864) for 15 minutes before counting using the Celigo Imaging Cell Cytometer (Brooks). Number of PI positive foci was normalized to cell number determined by Hoechst 33342 staining of a duplicate plate, followed by nuclei counting using Celigo Imaging Cell Cytometer (Brooks). Cell viability was assessed by incubating CellTiterGlo (Promega, G7570) with cells for 10 minutes in a 96-well plate and measuring luminescence with a plate reader (Molecular Devices). SUM159 cells were

treated with 50nM H3B-8800. Luminescence was normalized to cell number as described above.

Luminescent apoptosis assays—Caspase-3/7 and Caspase-8 activity was assessed in breast cancer lines by incubating Caspase-Glo 3/7 (Promega, G8090) and −8 (Promega, G8200) reagent with cells for one hour in a 96-well plate and measuring luminescence with a plate reader (Molecular Devices). SUM159 and LM2 cells were treated with 50nM H3B-8800 for 36 hours or with 200nM SD6 and 1ug/mL ZVAD, ZIETD, Z-AEVD, or Z-LEHD (R&D Systems) as annotated. MYC-ER HME1 cells were treated with 10nM 4-OHT and 20nM H3B-8800. 2208L, PyMT-M, AT3, and 2208L cells were treated with 50nM H3B-8800. Luminescence was normalized to cell number determined by Hoechst 33342 staining of a duplicate plate, followed by nuclei counting using the Celigo Imaging Cell Cytometer (Brooks).

MAVS immunofluorescence aggregation imaging and analysis—LM2 and SUM159 cells were treated with DMSO, 20nM H3B-8800, or .5ug/mL p (I:C) (Sigma Aldrich, P1530). High resolution imaging was performed on a GE Healthcare DVLive epifluorescence image restoration microscope using an Olympus PlanApo 60×/1.42 NA objective and a 1.9k × 1.9x sCMOS camera. Z stacks (0.25μm) were acquired before applying a conservative restorative algorithm for quantitative image deconvolution. Max intensity projections were generated and used for image analysis. To quantify the spatial distribution of the MAVS signal, we measured a dispersion index using a custom-made MATLAB script. Briefly, z-stacks were transformed into a 2D image by maximal projection. Single cells were then manually segmented using an interactive polygonal ROI. The dispersion index of the MAVS signal for each cell was then determined as follows: first, the MAVS signal was segmented using an Otsu thresholding method, and the weighted centroid location of the resulting mask was determined using the underlying pixel intensities. Then, the distance between each pixel of the MAVS mask to the weighted centroid was calculated and the dispersion index was defined as the mean of these distances. Aggregation was calculated as the inverse of the dispersion index.

Semi-Denaturing Detergent Agarose Gel Electrophoresis (SDD-AGE)—SUM159 and LM2 cells treated with DMSO or 20nM H3B-8800 were washed with ice-cold PBS and detached using a cell scraper. Cells were pelleted, resuspended in Buffer A (10mM Tris-HCl [pH 7.5], 10mM KCl, 1.5 mM $MgCl_2$, 0.25 M D-mannitol, and Roche EDTA-free protease inhibitor cocktail), and lysed by repeated douncing. Cellular debris was removed by centrifugation at 1000 × g for 5 minutes, and the supernatant was centrifuged at 10,000 × g for 10 minutes at 4°C to isolate the P5 mitochondrial fraction. SDD-AGE was performed according to a previously published protocol (Halfmann and Lindquist, 2008) with slight modifications. Crude P5 mitochondria was resuspended in 1 × sample buffer (0.5 × TBE, 10% glycerol, 2% SDS, and 0.0025% bromophenol blue) and run on a vertical agarose gel (1.5% agarose with 0.1% SDS in 1 × TBE) in running buffer (1 × TBE with 0.1% SDS) for 45 minutes at a constant 100 V in 4°C. Protein was transferred using capillary transfer overnight to a nitrocellulose membrane for immunoblotting.

In vivo tumor studies—Tumor chunks were transplanted into clear mammary fat pad of 4–5 week old female C57BL/6J or BALB/c AnNHsd female mice. 2208L, PyMT-M, and AT3 tumors were randomized onto vehicle or H3B-8800 (8 mg/kg in 0.5% methylcellulose daily) at 150–250mm^3 for long term response studies or 300–500mm^3 for short term studies. T11 tumors were randomized onto vehicle or H3B-8800 one day post tumor transplant. Tumor volume was measured using calipers three days per week. Tumors were harvested between 1500 and 2000 mm^3. Tissue chunks were stored in RNAlater for gene expression profiling. Tissue for IHC analysis was fixed in PFA, 70% EtOH, then paraffin embedded.

Immunohistochemistry (IHC) and quantification—Tumor chunks were fixed in 10% formalin overnight at 4°C overnight, and subsequently transferred into 70% ethanol, embedded in paraffin, and sectioned at regular intervals. Slides were deparaffinized and hydrated using xylene, graded ethyl alcohol, and dH2O. After antigen retrieval, 15 minutes of steaming at 90°C with pressure in 0.1M Tris-HCl, pH 9.0, sections were treated with 3% hydrogen peroxide solution for 5 minutes. Sections were incubated with primary antibody (CD8a, Cell Signaling 98941 diluted 1:100) for 1hr at RT. Sections were then incubated with Envision Labelled Polymer-HRP (Dako) for 30 minutes at RT. DAB+ solution (DakoCytomation) was then added to section, incubated for 15 minutes, followed by application of DAB Sparkle Enhancer (Biocare). Sections were counterstained with Harris Hematoxylin. Counting of CD8a+ stained cells was done using the Count Tool in Adobe Photoshop.

Immune signature single sample GSEA (ssGSEA)—Analysis of immune cell gene signatures was performed using single sample Gene Set Enrichment Analysis (Barbie *et al.*, 2009). Marker genes for immune cell types were obtained from (Bindea *et al.*, 2013). Heatmaps display z-score normalized IR levels and ssGSEA scores across samples, with “high” and “low” IR being defined as having an IR level outside one standard deviation of the mean.

TCGA intron retention and immune pathway analysis—Intron retention analysis was performed on BRCA TCGA RNA sequencing datasets (Koboldt et al., 2012). TCGA fastq reads were mapped using the STAR aligner (v2.3.1) (Dobin *et al.*, 2013) onto the hg19/GRCh37 reference genome as previously described (Hsu *et al.*, 2015). Level of intron retention (IR level) within each sample was calculated as the number of introns with IR scores > 0.01, as defined previously. “High” and “Low” IR were defined as having an IR level outside one standard deviation of the mean. RSEM normalized gene expression data from TCGA was obtained from the Broad GDAC Firehose. Copy number was obtained from cBioPortal as GISTIC2.0 data. Copy number analysis was done by segregating tumors based on a score of ≥ 1 (“High”) versus ≤ 0 (“Low” or normal). GSEA was performed using C2 Canonical Pathway annotations. TMB was obtained from GDC mutation data using the TCGAbiolinks R package (Colaprico et al., 2015). Survival data was obtained from the GDC portal and KM curves were plotted using the survminer R package. P-values were calculated using log-rank test.

QUANTIFICATION AND STATISTICAL ANALYSIS

Data are typically mean ± SEM. Data were analyzed by two-tailed unpaired Student's t-test between two groups, one-way ANOVA with Dunnett's multiple comparison test, or Mann-Whitney *U* test as appropriate. GraphPad Prism or R were used to generate all charts and statistical analyses. Statistical details of experiments, including statistical tests and sample sizes used, can be found in the figure legends. All experiments were performed on biological replicates unless otherwise specified.

Supplementary Material

Refer to Web version on PubMed Central for supplementary material.

Acknowledgements

E.A.B. and J.H.W. are supported by Baylor Research Advocates for Student Scientists and the NIH (T32GM120011, E.A.B.). F.G. is supported by CPRIT (RP160283). J.K.M. is supported by Susan G. Komen (PDF17487931). This project was supported by the Advanced Technology Cores at BCM: Genomic and RNA Profiling Core (NCI: CA125123), Cytometry and Cell Sorting Core (CPRIT-RP180672), and Integrated Microscopy Core (NIH: DK56338 and CA125123; CPRIT: RP150578 and RP170719). This work was supported by the Dan L. Duncan Comprehensive Cancer Center (NCI P30: CA125123) and Pathology Core of the Lester and Sue Smith Breast Center. The results shown here are based upon data generated by the TCGA Research Network: https://www.cancer.gov/tcga. I.G. is supported by the NIH (R01GM082837) and NSF (PHY-1147498, PHY-1430124, and PHY-1427654). J.H.W., W.W., X.H.-F.Z., and T.F.W. are supported by The McNair Medical Institute. X.H.-F.Z. and T.F.W. are supported by the DOD (1W81XWH-18-1-0573). T.F.W. is supported by the NIH and NCI (U01 CA214125, 1R01CA215226, 1R01CA215452), The Welch Foundation (Q-0007), prior research funding from H3Biomedicine, and the CRUK Grand Challenge and the Mark Foundation for Cancer Research (C5470/A27144 to T.F.W. as a member of the SPECIFICANCER Team).

References

Aird D, Teng T, Huang C-L, Pazolli E, Banka D, Cheung-Ong K, Eifert C, Furman C, Wu ZJ, Seiler M, et al. , 2019. Sensitivity to splicing modulation of BCL2 family genes defines cancer therapeutic strategies for splicing modulators. Nat. Commun 10, 137. [PubMed: 30635584]

Al-Kuraya K, Schraml P, Torhorst J, Tapia C, Zaharieva B, Novotny H, Spichtin H, Maurer R, Mirlacher M, Köchli O, et al. , 2004. Prognostic relevance of gene amplifications and coamplifications in breast cancer. Cancer Res. 64, 8534–8540. [PubMed: 15574759]

Andrejeva J, Childs KS, Young DF, Carlos TS, Stock N, Goodbourn S, Randall RE, 2004. The V proteins of paramyxoviruses bind the IFN-inducible RNA helicase, mda-5, and inhibit its activation of the IFN- promoter. Proc. Natl. Acad. Sci 101, 17264–17269. [PubMed: 15563593]

Arimoto K, Takahashi H, Hishiki T, Konishi H, Fujita T, Shimotohno K, 2007. Negative regulation of the RIG-I signaling by the ubiquitin ligase RNF125. Proc. Natl. Acad. Sci. U. S. A 104, 7500–5. [PubMed: 17460044]

Aulmann S, Adler N, Rom J, Helmchen B, Schirmacher P, Sinn HP, 2006. c-myc amplifications in primary breast carcinomas and their local recurrences. J. Clin. Pathol 59, 424–428. [PubMed: 16497871]

Bai B, Hales CM, Chen P-C, Gozal Y, Dammer EB, Fritz JJ, Wang X, Xia Q, Duong DM, Street C, et al. , 2013. U1 small nuclear ribonucleoprotein complex and RNA splicing alterations in Alzheimer's disease. Proc. Natl. Acad. Sci. U. S. A 110, 16562–7. [PubMed: 24023061]

Barbie DA, Tamayo P, Boehm JS, Kim SY, Moody SE, Dunn IF, Schinzel AC, Sandy P, Meylan E, Scholl C, et al. , 2009. Systematic RNA interference reveals that oncogenic KRAS-driven cancers require TBK1. Nature 462, 108–12. [PubMed: 19847166]

Berg MG, Wan L, Younis I, Diem MD, Soo M, Wang C, Dreyfuss G, 2012. A Quantitative High-Throughput In Vitro Splicing Assay Identifies Inhibitors of Spliceosome Catalysis. Mol. Cell. Biol 32, 1271–1283. [PubMed: 22252314]

Bernards R, Dessain SK, Weinberg RA, 1986. N-myc amplification causes down-modulation of MHC class I antigen expression in neuroblastoma. Cell 47, 667–674. [PubMed: 3096575]

Bezzi M, Teo SX, Muller J, Mok WC, Sahu SK, Vardy LA, Bonday ZQ, Guccione E, 2013. Regulation of constitutive and alternative splicing by PRMT5 reveals a role for Mdm4 pre-mRNA in sensing defects in the spliceosomal machinery. Genes Dev. 27, 1903–1916. [PubMed: 24013503]

Bindea G, Mlecnik B, Tosolini M, Kirilovsky A, Waldner M, Obenauf AC, Angell H, Fredriksen T, Lafontaine L, Berger A, et al. , 2013. Spatiotemporal dynamics of intratumoral immune cells reveal the immune landscape in human cancer. Immunity 39, 782–95. [PubMed: 24138885]

Braunschweig U, Barbosa-Morais NL, Pan Q, Nachman EN, Alipanahi B, Gonatopoulos-Pournatzis T, Frey B, Irimia M, Blencowe BJ, 2014. Widespread intron retention in mammals functionally tunes transcriptomes. Genome Res. 24, 1774–1786. [PubMed: 25258385]

Buckley PT, Khaladkar M, Kim J, Eberwine J, 2014. Cytoplasmic intron retention, function, splicing, and the sentinel RNA hypothesis. Wiley Interdiscip. Rev. RNA 5, 223–30. [PubMed: 24190870]

Casey SC, Baylot V, Felsher DW, 2017. MYC: Master Regulator of Immune Privilege. Trends Immunol.

Casey SC, Baylot V, Felsher DW, 2018. The MYC oncogene is a global regulator of the immune response. Blood.

Casey SC, Tong L, Li Y, Do R, Walz S, Fitzgerald KN, Gouw AM, Baylot V, Gutgemann I, Eilers M, et al. , 2016. MYC regulates the antitumor immune response through CD47 and PD-L1. Science (80-.). 352, 227–231.

Chan S, Sridhar P, Kirchner R, Lock YJ, Herbert Z, Buonamici S, Smith P, Lieberman J, Petrocca F, 2017. Basal-A Triple-Negative Breast Cancer Cells Selectively Rely on RNA Splicing for Survival. Mol. Cancer Ther 16, 2849–2861. [PubMed: 28878028]

Chiappinelli KB, Strissel PL, Desrichard A, Li H, Henke C, Akman B, Hein A, Rote NS, Cope LM, Snyder A, et al. , 2015. Inhibiting DNA Methylation Causes an Interferon Response in Cancer via dsRNA Including Endogenous Retroviruses. Cell 162, 974–986. [PubMed: 26317466]

Colaprico A, Silva TC, Olsen C, Garofano L, Cava C, Garolini D, Sabedot TS, Malta TM, Pagnotta SM, Castiglioni I, et al. , 2015. TCGAbiolinks: an R/Bioconductor package for integrative analysis of TCGA data. Nucleic Acids Res. 44, e71–e71. [PubMed: 26704973]

Courtneidge SA, Smith AE, 1983. Polyoma virus transforming protein associates with the product of the c-src cellular gene. Nature 303, 435–439. [PubMed: 6304524]

Cristescu R, Mogg R, Ayers M, Albright A, Murphy E, Yearley J, Sher X, Liu XQ, Lu H, Nebozhyn M, et al. , 2018. Pan-tumor genomic biomarkers for PD-1 checkpoint blockade–based immunotherapy. Science (80-.). 362, eaar3593.

Darman RB, Seiler M, Agrawal AA, Lim KH, Peng S, Aird D, Bailey SL, Bhavsar EB, Chan B, Colla S, et al. , 2015. Cancer-Associated SF3B1 Hotspot Mutations Induce Cryptic 3' Splice Site Selection through Use of a Different Branch Point. Cell Rep. 13, 1033–45. [PubMed: 26565915]

Das S, Anczuków O, Akerman M, Krainer AR, 2012. Oncogenic splicing factor SRSF1 is a critical transcriptional target of MYC. Cell Rep. 1, 110–7. [PubMed: 22545246]

David CJ, Chen M, Assanah M, Canoll P, Manley JL, 2010. HnRNP proteins controlled by c-Myc deregulate pyruvate kinase mRNA splicing in cancer. Nature 463, 364–8. [PubMed: 20010808]

DeBoever C, Ghia EM, Shepard PJ, Rassenti L, Barrett CL, Jepsen K, Jamieson CHM, Carson D, Kipps TJ, Frazer KA, 2015. Transcriptome sequencing reveals potential mechanism of cryptic 3' splice site selection in SF3B1-mutated cancers. PLoS Comput. Biol 11, e1004105.

Deming SL, Nass SJ, Dickson RB, Trock BJ, 2000. C-myc amplification in breast cancer: A meta-analysis of its occurrence and prognostic relevance. Br. J. Cancer 83, 1688–1695. [PubMed: 11104567]

Der SD, Yang Y-L, Weissmann C, Williams BRG, 1997. A double-stranded RNA-activated protein kinase-dependent pathway mediating stress-induced apoptosis. Proc. Natl. Acad. Sci 94, 3279–3283. [PubMed: 9096384]

Dobin A, Davis CA, Schlesinger F, Drenkow J, Zaleski C, Jha S, Batut P, Chaisson M, Gingeras TR, 2013. STAR: ultrafast universal RNA-seq aligner. Bioinformatics 29, 15–21. [PubMed: 23104886]

Doma MK, Parker R, 2007. RNA Quality Control in Eukaryotes. Cell 131, 660–668. [PubMed: 18022361]

Dvinge H, Bradley RK, 2015. Widespread intron retention diversifies most cancer transcriptomes. Genome Med. 7, 45. [PubMed: 26113877]

El Maadidi S, Faletti L, Berg B, Wenzl C, Wieland K, Chen ZJ, Maurer U, Borner C, 2014. A Novel Mitochondrial MAVS/Caspase-8 Platform Links RNA Virus-Induced Innate Antiviral Signaling to Bax/Bak-Independent Apoptosis. J. Immunol 192, 1171–1183. [PubMed: 24391214]

Elion DL, Jacobson ME, Hicks DJ, Rahman B, Sanchez V, Gonzales-Ericsson PI, Fedorova O, Pyle AM, Wilson JT, Cook RS, 2018. Therapeutically Active RIG-I Agonist Induces Immunogenic Tumor Cell Killing in Breast Cancers. Cancer Res. 78, 6183–6195. [PubMed: 30224377]

Elmore S, 2007. Apoptosis: a review of programmed cell death. Toxicol. Pathol 35, 495–516. [PubMed: 17562483]

Gannon HS, Zou T, Kiessling MK, Gao GF, Cai D, Choi PS, Ivan AP, Buchumenski I, Berger AC, Goldstein JT, et al. , 2018. Identification of ADAR1 adenosine deaminase dependency in a subset of cancer cells. Nat. Commun 9, 5450. [PubMed: 30575730]

Gil J, Esteban M, 2000. Induction of apoptosis by the dsRNA-dependent protein kinase (PKR): mechanism of action. Apoptosis 5, 107–14. [PubMed: 11232238]

Goodman AM, Kato S, Bazhenova L, Patel SP, Frampton GM, Miller V, Stephens PJ, Daniels GA, Kurzrock R, 2017. Tumor Mutational Burden as an Independent Predictor of Response to Immunotherapy in Diverse Cancers. Mol. Cancer Ther 16, 2598–2608. [PubMed: 28835386]

Goubau D, Schlee M, Deddouche S, Pruijssers AJ, Zillinger T, Goldeck M, Schuberth C, Van der Veen AG, Fujimura T, Rehwinkel J, et al. , 2014. Antiviral immunity via RIG-I-mediated recognition of RNA bearing 5′-diphosphates. Nature 514, 372–375. [PubMed: 25119032]

Graubert TA, Shen D, Ding L, Okeyo-Owuor T, Lunn CL, Shao J, Krysiak K, Harris CC, Koboldt DC, Larson DE, et al. , 2012. Recurrent mutations in the U2AF1 splicing factor in myelodysplastic syndromes. Nat. Genet 44, 53–57.

Halfmann R, Lindquist S, 2008. Screening for amyloid aggregation by Semi-Denaturing Detergent-Agarose Gel Electrophoresis. J. Vis. Exp

Han T, Goralski M, Gaskill N, Capota E, Kim J, Ting TC, Xie Y, Williams NS, Nijhawan D, 2017. Anticancer sulfonamides target splicing by inducing RBM39 degradation via recruitment to DCAF15. Science 356, eaal3755.

Hornung V, Ellegast J, Kim S, Brzozka K, Jung A, Kato H, Poeck H, Akira S, Conzelmann K-K, Schlee M, et al. , 2006. 5'-Triphosphate RNA Is the Ligand for RIG-I. Science (80-.). 314, 994–997.

Hou F, Sun L, Zheng H, Skaug B, Jiang Q-X, Chen ZJ, 2011. MAVS Forms Functional Prion-like Aggregates to Activate and Propagate Antiviral Innate Immune Response. Cell 146, 448–461. [PubMed: 21782231]

Hsu TY-T, Simon LM, Neill NJ, Marcotte R, Sayad A, Bland CS, Echeverria GV, Sun T, Kurley SJ, Tyagi S, et al. , 2015. The spliceosome is a therapeutic vulnerability in MYC-driven cancer. Nature 525, 384–388. [PubMed: 26331541]

Hubert CG, Bradley RK, Ding Y, Toledo CM, Herman J, Skutt-Kakaria K, Girard EJ, Davison J, Berndt J, Corrin P, et al. , 2013. Genome-wide RNAi screens in human brain tumor isolates reveal a novel viability requirement for PHF5A. Genes Dev. 27, 1032–1045. [PubMed: 23651857]

Hugo W, Zaretsky JM, Sun L, Song C, Moreno BH, Hu-Lieskovan S, Berent-Maoz B, Pang J, Chmielowski B, Cherry G, et al. , 2016. Genomic and Transcriptomic Features of Response to Anti-PD-1 Therapy in Metastatic Melanoma. Cell 165, 35–44. [PubMed: 26997480]

Iordanov MS, Ryabinina OP, Schneider P, Magun BE, 2005. Two mechanisms of caspase 9 processing in double-stranded RNA- and virus-triggered apoptosis. Apoptosis 10, 153–66. [PubMed: 15711931]

Ishizuka JJ, Manguso RT, Cheruiyot CK, Bi K, Panda A, Iracheta-Vellve A, Miller BC, Du PP, Yates KB, Dubrot J, et al. , 2019. Loss of ADAR1 in tumours overcomes resistance to immune checkpoint blockade. Nature 565, 43–48. [PubMed: 30559380]

Kahles A, Lehmann K-V, Toussaint NC, Hüser M, Stark SG, Sachsenberg T, Stegle O, Kohlbacher O, Sander C, Cancer Genome Atlas Research Network, et al. , 2018. Comprehensive Analysis of Alternative Splicing Across Tumors from 8,705 Patients. Cancer Cell 34, 211–224.e6.

Kaida D, Motoyoshi H, Tashiro E, Nojima T, Hagiwara M, Ishigami K, Watanabe H, Kitahara T, Yoshida T, Nakajima H, et al. , 2007. Spliceostatin A targets SF3b and inhibits both splicing and nuclear retention of pre-mRNA. Nat. Chem. Biol 3, 576–83. [PubMed: 17643111]

Kang D, Gopalkrishnan RV, Wu Q, Jankowsky E, Pyle AM, Fisher PB, 2002. mda-5: An interferon-inducible putative RNA helicase with double-stranded RNA-dependent ATPase activity and melanoma growth-suppressive properties. Proc. Natl. Acad. Sci. U. S. A 99, 637–42. [PubMed: 11805321]

Kato H, Takeuchi O, Mikamo-Satoh E, Hirai R, Kawai T, Matsushita K, Hiiragi A, Dermody TS, Fujita T, Akira S, 2008. Length-dependent recognition of double-stranded ribonucleic acids by retinoic acid-inducible gene-I and melanoma differentiation-associated gene 5. J. Exp. Med 205, 1601–10. [PubMed: 18591409]

Kawai T, Takahashi K, Sato S, Coban C, Kumar H, Kato H, Ishii KJ, Takeuchi O, Akira S, 2005. IPS-1, an adaptor triggering RIG-I- and Mda5-mediated type I interferon induction. Nat. Immunol 6, 981–8. [PubMed: 16127453]

Kessler JD, Kahle KT, Sun T, Meerbrey KL, Schlabach MR, Schmitt EM, Skinner SO, Xu Q, Li MZ, Hartman ZC, et al. , 2012. A SUMOylation-Dependent Transcriptional Subprogram Is Required for Myc-Driven Tumorigenesis. Science (80-.). 335, 348–353.

Kibler KV, Shors T, Perkins KB, Zeman CC, Banaszak MP, Biesterfeldt J, Langland JO, Jacobs BL, 1997. Double-stranded RNA is a trigger for apoptosis in vaccinia virus-infected cells. J. Virol 71, 1992–2003. [PubMed: 9032331]

Kim D, Langmead B, Salzberg SL, 2015. HISAT: a fast spliced aligner with low memory requirements. Nat. Methods 12, 357–60. [PubMed: 25751142]

Kim E, Ilagan JO, Liang Y, Daubner GM, Lee SC-W, Ramakrishnan A, Li Y, Chung YR, Micol J-B, Murphy ME, et al. , 2015. SRSF2 Mutations Contribute to Myelodysplasia by Mutant-Specific Effects on Exon Recognition. Cancer Cell 27, 617–630. [PubMed: 25965569]

Koboldt DC, Fulton RS, McLellan MD, Schmidt H, Kalicki-Veizer J, McMichael JF, Fulton LL, Dooling DJ, Ding L, Mardis ER, et al. , 2012. Comprehensive molecular portraits of human breast tumours. Nature 490, 61–70. [PubMed: 23000897]

Koh CM, Bezzi M, Low DHP, Ang WX, Teo SX, Gay FPH, Al-Haddawi M, Tan SY, Osato M, Sabò A, et al. , 2015. MYC regulates the core pre-mRNA splicing machinery as an essential step in lymphomagenesis. Nature 523, 96–100. [PubMed: 25970242]

Kortlever RM, Sodir NM, Wilson CH, Burkhart DL, Pellegrinet L, Brown Swigart L, Littlewood TD, Evan GI, 2017. Myc Cooperates with Ras by Programming Inflammation and Immune Suppression. Cell 171, 1301–1315.e14.

Lagisetti C, Palacios G, Goronga T, Freeman B, Caufield W, Webb TR, 2013. Optimization of antitumor modulators of pre-mRNA splicing. J. Med. Chem 56, 10033–10044. [PubMed: 24325474]

Langmead B, Salzberg SL, 2012. Fast gapped-read alignment with Bowtie 2. Nat. Methods 9, 357–359. [PubMed: 22388286]

Larrayoz M, Blakemore SJ, Dobson RC, Blunt MD, Rose-Zerilli MJJ, Walewska R, Duncombe A, Oscier D, Koide K, Forconi F, et al. , 2016. The SF3B1 inhibitor spliceostatin A (SSA) elicits apoptosis in chronic lymphocytic leukaemia cells through downregulation of Mcl-1. Leukemia 30, 351–360. [PubMed: 26488112]

Lee SC-W, Dvinge H, Kim E, Cho H, Micol J-B, Chung YR, Durham BH, Yoshimi A, Kim YJ, Thomas M, et al. , 2016. Modulation of splicing catalysis for therapeutic targeting of leukemia with mutations in genes encoding spliceosomal proteins. Nat. Med 22, 672–8. [PubMed: 27135740]

Lei Y, Moore CB, Liesman RM, O'Connor BP, Bergstralh DT, Chen ZJ, Pickles RJ, Ting JPY, 2009. MAVS-Mediated Apoptosis and Its Inhibition by Viral Proteins. PLoS One 4.

Li D, Xie P, Zhao F, Shu J, Li L, Zhan Y, Zhang L, 2015. F-box protein Fbxo3 targets Smurf1 ubiquitin ligase for ubiquitination and degradation. Biochem. Biophys. Res. Commun 458, 941–945. [PubMed: 25721664]

Li H, Handsaker B, Wysoker A, Fennell T, Ruan J, Homer N, Marth G, Abecasis G, Durbin R, 2009. The Sequence Alignment/Map format and SAMtools. Bioinformatics 25, 2078–2079. [PubMed: 19505943]

Liao Y, Smyth GK, Shi W, 2014. featureCounts: an efficient general purpose program for assigning sequence reads to genomic features. Bioinformatics 30, 923–930. [PubMed: 24227677]

Liberzon A, Subramanian A, Pinchback R, Thorvaldsdóttir H, Tamayo P, Mesirov JP, 2011. Molecular signatures database (MSigDB) 3.0. Bioinformatics 27, 1739–1740. [PubMed: 21546393]

Lin CY, Lovén J, Rahl PB, Paranal RM, Burge CB, Bradner JE, Lee TI, Young RA, 2012. Transcriptional amplification in tumor cells with elevated c-Myc. Cell 151, 56–67. [PubMed: 23021215]

Linehan MM, Dickey TH, Molinari ES, Fitzgerald ME, Potapova O, Iwasaki A, Pyle AM, 2018. A minimal RNA ligand for potent RIG-I activation in living mice. Sci. Adv 4, e1701854.

Liu H, Golji J, Brodeur LK, Chung FS, Chen JT, DeBeaumont RS, Bullock CP, Jones MD, Kerr G, Li L, et al. , 2018. Tumor-derived IFN triggers chronic pathway agonism and sensitivity to ADAR loss. Nat. Med 25, 95–102. [PubMed: 30559422]

Liu Y, Lu N, Yuan B, Weng L, Wang F, Liu Y-J, Zhang Z, 2014. The interaction between the helicase DHX33 and IPS-1 as a novel pathway to sense double-stranded RNA and RNA viruses in myeloid dendritic cells. Cell. Mol. Immunol 11, 49–57. [PubMed: 24037184]

Love MI, Huber W, Anders S, 2014. Moderated estimation of fold change and dispersion for RNA-seq data with DESeq2. Genome Biol. 15, 550. [PubMed: 25516281]

Luo N, Nixon MJ, Gonzalez-Ericsson PI, Sanchez V, Opalenik SR, Li H, Zahnow CA, Nickels ML, Liu F, Tantawy MN, et al., 2018. DNA methyltransferase inhibition upregulates MHC-I to potentiate cytotoxic T lymphocyte responses in breast cancer. 9, 248.

Mallampalli RK, Coon TA, Glasser JR, Wang C, Dunn SR, Weathington NM, Zhao J, Zou C, Zhao Y, Chen BB, 2013. Targeting F box protein Fbxo3 to control cytokine-driven inflammation. J. Immunol 191, 5247–55. [PubMed: 24123678]

Martin M, 2011. Cutadapt removes adapter sequences from high-throughput sequencing reads. EMBnet.journal 17, 10.

McGranahan N, Furness AJS, Rosenthal R, Ramskov S, Lyngaa R, Saini SK, Jamal-Hanjani M, Wilson GA, Birkbak NJ, Hiley CT, et al. , 2016. Clonal neoantigens elicit T cell immunoreactivity and sensitivity to immune checkpoint blockade. Science (80-.). 351, 1463–1469.

Meerbrey KL, Hu G, Kessler JD, Roarty K, Li MZ, Fang JE, Herschkowitz JI, Burrows AE, Ciccia A, Sun T, et al. , 2011. The pINDUCER lentiviral toolkit for inducible RNA interference in vitro and in vivo. Proc. Natl. Acad. Sci 108, 3665–3670. [PubMed: 21307310]

Mehdipour P, Marhon SA, Ettayebi I, Chakravarthy A, Hosseini A, Wang Y, de Castro FA, Loo Yau H, Ishak C, Abelson S, et al. , 2020. Epigenetic therapy induces transcription of inverted SINEs and ADAR1 dependency. Nature.

Meylan E, Curran J, Hofmann K, Moradpour D, Binder M, Bartenschlager R, Tschopp J, 2005. Cardif is an adaptor protein in the RIG-I antiviral pathway and is targeted by hepatitis C virus. Nature 437, 1167–1172. [PubMed: 16177806]

Minn AJ, Gupta GP, Siegel PM, Bos PD, Shu W, Giri DD, Viale A, Olshen AB, Gerald WL, Massagué J, 2005. Genes that mediate breast cancer metastasis to lung. Nature 436, 518–524. [PubMed: 16049480]

Moore MJ, Wang Q, Kennedy CJ, Silver PA, 2010. An Alternative Splicing Network Links Cell-Cycle Control to Apoptosis. Cell 142, 625–636. [PubMed: 20705336]

Nabet B, Roberts JM, Buckley DL, Paulk J, Dastjerdi S, Yang A, Leggett AL, Erb MA, Lawlor MA, Souza A, et al. , 2018. The dTAG system for immediate and target-specific protein degradation. Nat. Chem. Biol 14, 431–441. [PubMed: 29581585]

Nakajima H, Hori Y, Terano H, Okuhara M, Manda T, Matsumoto S, Shimomura K, 1996. New antitumor substances, FR901463, FR901464 and FR901465. II. Activities against experimental tumors in mice and mechanism of action. J. Antibiot. (Tokyo) 49, 1204–11. [PubMed: 9031665]

Obeng EA, Chappell RJ, Seiler M, Chen MC, Campagna DR, Schmidt PJ, Schneider RK, Lord AM, Wang L, Gambe RG, et al. , 2016. Physiologic Expression of Sf3b1(K700E) Causes Impaired

Erythropoiesis, Aberrant Splicing, and Sensitivity to Therapeutic Spliceosome Modulation. Cancer Cell 30, 404–417. [PubMed: 27622333]

Pawellek A, McElroy S, Samatov T, Mitchell L, Woodland A, Ryder U, Gray D, Lührmann R, Lamond AI, 2014. Identification of Small Molecule Inhibitors of Pre-mRNA Splicing. J. Biol. Chem 289, 34683–34698. [PubMed: 25281741]

Popp MW-L, Maquat LE, 2013. Organizing principles of mammalian nonsense-mediated mRNA decay. Annu. Rev. Genet 47, 139–65. [PubMed: 24274751]

Raj T, Li YI, Wong G, Humphrey J, Wang M, Ramdhani S, Wang Y-C, Ng B, Gupta I, Haroutunian V, et al. , 2018. Integrative transcriptome analyses of the aging brain implicate altered splicing in Alzheimer's disease susceptibility. Nat. Genet 50, 1584–1592. [PubMed: 30297968]

Rizvi NA, Hellmann MD, Snyder A, Kvistborg P, Makarov V, Havel JJ, Lee W, Yuan J, Wong P, Ho TS, et al. , 2015. Mutational landscape determines sensitivity to PD-1 blockade in non-small cell lung cancer. Science (80-.). 348, 124–128.

Robanus-Maandag EC, Bosch CAJ, Kristel PM, Hart AAM, Faneyte IF, Nederlof PM, Peterse JL, van de Vijver MJ, 2003. Association of C-MYC amplification with progression from the in situ to the invasive stage in C-MYC-amplified breast carcinomas. J. Pathol 201, 75–82. [PubMed: 12950019]

Rooney MS, Shukla SA, Wu CJ, Getz G, Hacohen N, 2015. Molecular and genetic properties of tumors associated with local immune cytolytic activity. Cell 160, 48–61. [PubMed: 25594174]

Roulois D, Loo Yau H, Singhania R, Wang Y, Danesh A, Shen SY, Han H, Liang G, Jones PA, Pugh TJ, et al. , 2015. DNA-Demethylating Agents Target Colorectal Cancer Cells by Inducing Viral Mimicry by Endogenous Transcripts. Cell 162, 961–73. [PubMed: 26317465]

Rousseaux MWC, Vázquez-Vélez GE, Al-Ramahi I, Jeong HH, Bajić A, Revelli JP, Ye H, Phan ET, Deger JM, Perez AM, et al. , 2018. A druggable genome screen identifies modifiers of α-synuclein levels via a tiered cross-species validation approach. J. Neurosci 38, 9286–9301. [PubMed: 30249792]

Saldi TK, Ash PE, Wilson G, Gonzales P, Garrido-Lecca A, Roberts CM, Dostal V, Gendron TF, Stein LD, Blumenthal T, et al. , 2014. TDP-1, the *Caenorhabditis elegans* ortholog of TDP-43, limits the accumulation of double-stranded RNA. EMBO J. 33, 2947–2966. [PubMed: 25391662]

Schlotter CM, Vogt U, Bosse U, Mersch B, Waßmann K, 2003. C-myc, not HER-2/neu, can predict recurrence and mortality of patients with node-negative breast cancer. Breast Cancer Res. 5.

Schmidt A, Schwerd T, Hamm W, Hellmuth JC, Cui S, Wenzel M, Hoffmann FS, Michallet M-C, Besch R, Hopfner K-P, et al. , 2009. 5'-triphosphate RNA requires base-paired structures to activate antiviral signaling via RIG-I. Proc. Natl. Acad. Sci 106, 12067–12072. [PubMed: 19574455]

Schönborn J, Oberstrass J, Breyel E, Tittgen J, Schumacher J, Lukacs N, 1991. Monoclonal antibodies to double-stranded RNA as probes of RNA structure in crude nucleic acid extracts. Nucleic Acids Res. 19, 2993–3000. [PubMed: 2057357]

Sears N, Sen GC, Stark GR, Chattopadhyay S, 2011. Caspase-8-mediated Cleavage Inhibits IRF-3 Protein by Facilitating Its Proteasome-mediated Degradation. J. Biol. Chem 286, 33037–33044. [PubMed: 21816816]

Seiler M, Peng S, Agrawal AA, Palacino J, Teng T, Zhu P, Smith PG, Buonamici S, Yu L, Caesar-Johnson SJ, et al. , 2018a. Somatic Mutational Landscape of Splicing Factor Genes and Their Functional Consequences across 33 Cancer Types. Cell Rep. 23, 282–296.e4.

Seiler M, Yoshimi A, Darman R, Chan B, Keaney G, Thomas M, Agrawal AA, Caleb B, Csibi A, Sean E, et al. , 2018b. H3B-8800, an orally available small-molecule splicing modulator, induces lethality in spliceosome-mutant cancers. Nat. Med 24, 497–504. [PubMed: 29457796]

Sela N, Mersch B, Gal-Mark N, Lev-Maor G, Hotz-Wagenblatt A, Ast G, 2007. Comparative analysis of transposed element insertion within human and mouse genomes reveals Alu's unique role in shaping the human transcriptome. Genome Biol. 8, R127. [PubMed: 17594509]

Seth RB, Sun L, Ea C-K, Chen ZJ, 2005. Identification and characterization of MAVS, a mitochondrial antiviral signaling protein that activates NF-kappaB and IRF 3. Cell 122, 669–82. [PubMed: 16125763]

Sharma P, Hu-Lieskovan S, Wargo JA, Ribas A, 2017. Primary, Adaptive, and Acquired Resistance to Cancer Immunotherapy. Cell 168, 707–723. [PubMed: 28187290]

Shirai CL, White BS, Tripathi M, Tapia R, Ley JN, Ndonwi M, Kim S, Shao J, Carver A, Saez B, et al. , 2017. Mutant U2AF1-expressing cells are sensitive to pharmacological modulation of the spliceosome. Nat. Commun 8, 14060. [PubMed: 28067246]

Sidarovich A, Will CL, Anokhina MM, Ceballos J, Sievers S, Agafonov DE, Samatov T, Bao P, Kastner B, Urlaub H, et al. , 2017. Identification of a small molecule inhibitor that stalls splicing at an early step of spliceosome activation. Elife 6.

Smart AC, Margolis CA, Pimentel H, He MX, Miao D, Adeegbe D, Fugmann T, Wong KK, Van Allen EM, 2018. Intron retention is a source of neoepitopes in cancer. Nat. Biotechnol 36, 1056–1058. [PubMed: 30114007]

Snyder A, Makarov V, Merghoub T, Yuan J, Zaretsky JM, Desrichard A, Walsh LA, Postow MA, Wong P, Ho TS, et al. , 2014. Genetic basis for clinical response to CTLA-4 blockade in melanoma. N. Engl. J. Med 371, 2189–2199. [PubMed: 25409260]

Song G, Liu B, Li Z, Wu H, Wang P, Zhao K, Jiang G, Zhang L, Gao C, 2016. E3 ubiquitin ligase RNF128 promotes innate antiviral immunity through K63-linked ubiquitination of TBK1. Nat. Immunol 17, 1342–1351. [PubMed: 27776110]

Stone ML, Chiappinelli KB, Li H, Murphy LM, Travers ME, Topper MJ, Mathios D, Lim M, Shih I-M, Wang T-L, et al. , 2017. Epigenetic therapy activates type I interferon signaling in murine ovarian cancer to reduce immunosuppression and tumor burden. Proc. Natl. Acad. Sci. U. S. A 114, E10981–E10990. [PubMed: 29203668]

Subramanian A, Tamayo P, Mootha VK, Mukherjee S, Ebert BL, Gillette MA, Paulovich A, Pomeroy SL, Golub TR, Lander ES, et al. , 2005. Gene set enrichment analysis: A knowledge-based approach for interpreting genome-wide expression profiles. Proc. Natl. Acad. Sci 102, 15545–15550. [PubMed: 16199517]

Sumpter R, Loo Y-M, Foy E, Li K, Yoneyama M, Fujita T, Lemon SM, Gale M, 2005. Regulating Intracellular Antiviral Defense and Permissiveness to Hepatitis C Virus RNA Replication through a Cellular RNA Helicase, RIG-I. J. Virol 79, 2689–2699. [PubMed: 15708988]

Sun L, Fazal FM, Li P, Broughton JP, Lee B, Tang L, Huang W, Kool ET, Chang HY, Zhang QC, 2019. RNA structure maps across mammalian cellular compartments. Nat. Struct. Mol. Biol 26, 322–330. [PubMed: 30886404]

Szklarczyk D, Gable AL, Lyon D, Junge A, Wyder S, Huerta-Cepas J, Simonovic M, Doncheva NT, Morris JH, Bork P, et al. , 2019. STRING v11: Protein-protein association networks with increased coverage, supporting functional discovery in genome-wide experimental datasets. Nucleic Acids Res. 47, D607–D613. [PubMed: 30476243]

Takahashi K, Kawai T, Kumar H, Sato S, Yonehara S, Akira S, 2006. Roles of caspase-8 and caspase-10 in innate immune responses to double-stranded RNA. J. Immunol 176, 4520–4. [PubMed: 16585540]

Topper MJ, Vaz M, Chiappinelli KB, DeStefano Shields CE, Niknafs N, Yen R-WC, Wenzel A, Hicks J, Ballew M, Stone M, et al. , 2017. Epigenetic Therapy Ties MYC Depletion to Reversing Immune Evasion and Treating Lung Cancer. Cell 171, 1284–1300.e21.

Trapnell C, Williams BA, Pertea G, Mortazavi A, Kwan G, van Baren MJ, Salzberg SL, Wold BJ, Pachter L, 2010. Transcript assembly and quantification by RNA-Seq reveals unannotated transcripts and isoform switching during cell differentiation. Nat. Biotechnol 28, 511–5. [PubMed: 20436464]

Tsang JL, Jia SH, Parodo J, Plant P, Lodyga M, Charbonney E, Szaszi K, Kapus A, Marshall JC, 2016. Tyrosine Phosphorylation of Caspase-8 Abrogates Its Apoptotic Activity and Promotes Activation of c-Src. PLoS One 11, e0153946.

Uehara T, Minoshima Y, Sagane K, Sugi NH, Mitsuhashi KO, Yamamoto N, Kamiyama H, Takahashi K, Kotake Y, Uesugi M, et al. , 2017. Selective degradation of splicing factor CAPERα by anticancer sulfonamides. Nat. Chem. Biol 13, 675–680. [PubMed: 28437394]

Vaquero-Garcia J, Barrera A, Gazzara MR, González-Vallinas J, Lahens NF, Hogenesch JB, Lynch KW, Barash Y, 2016. A new view of transcriptome complexity and regulation through the lens of local splicing variations. Elife 5, e11752. [PubMed: 26829591]

Venables JP, 2004. Aberrant and alternative splicing in cancer. Cancer Res. 64, 7647–54. [PubMed: 15520162]

Wang L, Brooks AN, Fan J, Wan Y, Gambe R, Li S, Hergert S, Yin S, Freeman SS, Levin JZ, et al. , 2016. Transcriptomic Characterization of SF3B1 Mutation Reveals Its Pleiotropic Effects in Chronic Lymphocytic Leukemia. Cancer Cell 30, 750–763. [PubMed: 27818134]

Wang T, Wei JJ, Sabatini DM, Lander ES, 2014. Genetic screens in human cells using the CRISPR-Cas9 system. Science (80-.). 343, 80–84.

Wong JJ-L, Ritchie W, Ebner OA, Selbach M, Wong JWH, Huang Y, Gao D, Pinello N, Gonzalez M, Baidya K, et al. , 2013. Orchestrated intron retention regulates normal granulocyte differentiation. Cell 154, 583–95. [PubMed: 23911323]

Wyss-Coray T, 2006. Inflammation in Alzheimer disease: driving force, bystander or beneficial response? Nat. Med 12, 1005–1015. [PubMed: 16960575]

Xu L-G, Wang Y-Y, Han K-J, Li L-Y, Zhai Z, Shu H-B, 2005. VISA is an adapter protein required for virus-triggered IFN-beta signaling. Mol. Cell 19, 727–40. [PubMed: 16153868]

Yarchoan M, Hopkins A, Jaffee EM, 2017. Tumor Mutational Burden and Response Rate to PD-1 Inhibition. N. Engl. J. Med 377, 2500–2501. [PubMed: 29262275]

Yokoi A, Kotake Y, Takahashi K, Kadowaki T, Matsumoto Y, Minoshima Y, Sugi NH, Sagane K, Hamaguchi M, Iwata M, et al. , 2011. Biological validation that SF3b is a target of the antitumor macrolide pladienolide. FEBS J. 278, 4870–4880. [PubMed: 21981285]

Yoneyama M, Kikuchi M, Natsukawa T, Shinobu N, Imaizumi T, Miyagishi M, Taira K, Akira S, Fujita T, 2004. The RNA helicase RIG-I has an essential function in double-stranded RNA-induced innate antiviral responses. Nat. Immunol 5, 730–737. [PubMed: 15208624]

Yoshimoto R, Kaida D, Furuno M, Burroughs AM, Noma S, Suzuki H, Kawamura Y, Hayashizaki Y, Mayeda A, Yoshida M, 2017. Global analysis of pre-mRNA subcellular localization following splicing inhibition by spliceostatin A. RNA 23, 47–57. [PubMed: 27754875]

Yu G, 2018. Using meshes for MeSH term enrichment and semantic analyses. Bioinformatics 34, 3766–3767. [PubMed: 29790928]

Yu Z, Song H, Jia M, Zhang J, Wang W, Li Q, Zhang L, Zhao W, 2017. USP1–UAF1 deubiquitinase complex stabilizes TBK1 and enhances antiviral responses. J. Exp. Med 214, 3553–3563. [PubMed: 29138248]

Zeng W, Xu M, Liu S, Sun L, Chen ZJ, 2009. Key Role of Ubc5 and Lysine-63 Polyubiquitination in Viral Activation of IRF3. Mol. Cell 36, 315–325. [PubMed: 19854139]

Zhang J, Lieu YK, Ali AM, Penson A, Reggio KS, Rabadan R, Raza A, Mukherjee S, Manley JL, 2015. Disease-associated mutation in SRSF2 misregulates splicing by altering RNA-binding affinities. Proc. Natl. Acad. Sci 112, E4726–E4734. [PubMed: 26261309]

Zhang J, Manley JL, 2013. Misregulation of pre-mRNA alternative splicing in cancer. Cancer Discov.

Zhang Z, Kim T, Bao M, Facchinetti V, Jung SYY, Ghaffari AAA, Qin J, Cheng G, Liu Y-J, 2011a. DDX1, DDX21, and DHX36 helicases form a complex with the adaptor molecule TRIF to sense dsRNA in dendritic cells. Immunity 34, 866–78. [PubMed: 21703541]

Zhang Z, Yuan B, Lu N, Facchinetti V, Liu Y-J, 2011b. DHX9 Pairs with IPS-1 To Sense Double-Stranded RNA in Myeloid Dendritic Cells. J. Immunol 187, 4501. [PubMed: 21957149]

Zhou Y, Zhou B, Pache L, Chang M, Khodabakhshi AH, Tanaseichuk O, Benner C, Chanda SK, 2019. Metascape provides a biologist-oriented resource for the analysis of systems-level datasets. Nat. Commun 10, 1–10. [PubMed: 30602773]

Highlights

- Spliceosome-targeted therapies (STTs) induce widespread mis-spliced mRNA in cancer
- Mis-spliced, intron-retained mRNAs are an unexplored source of endogenous dsRNA
- STTs trigger antiviral signaling and extrinsic apoptosis in TNBCs via dsRNA sensors
- RNA mis-splicing in human breast cancers correlates with immune signatures

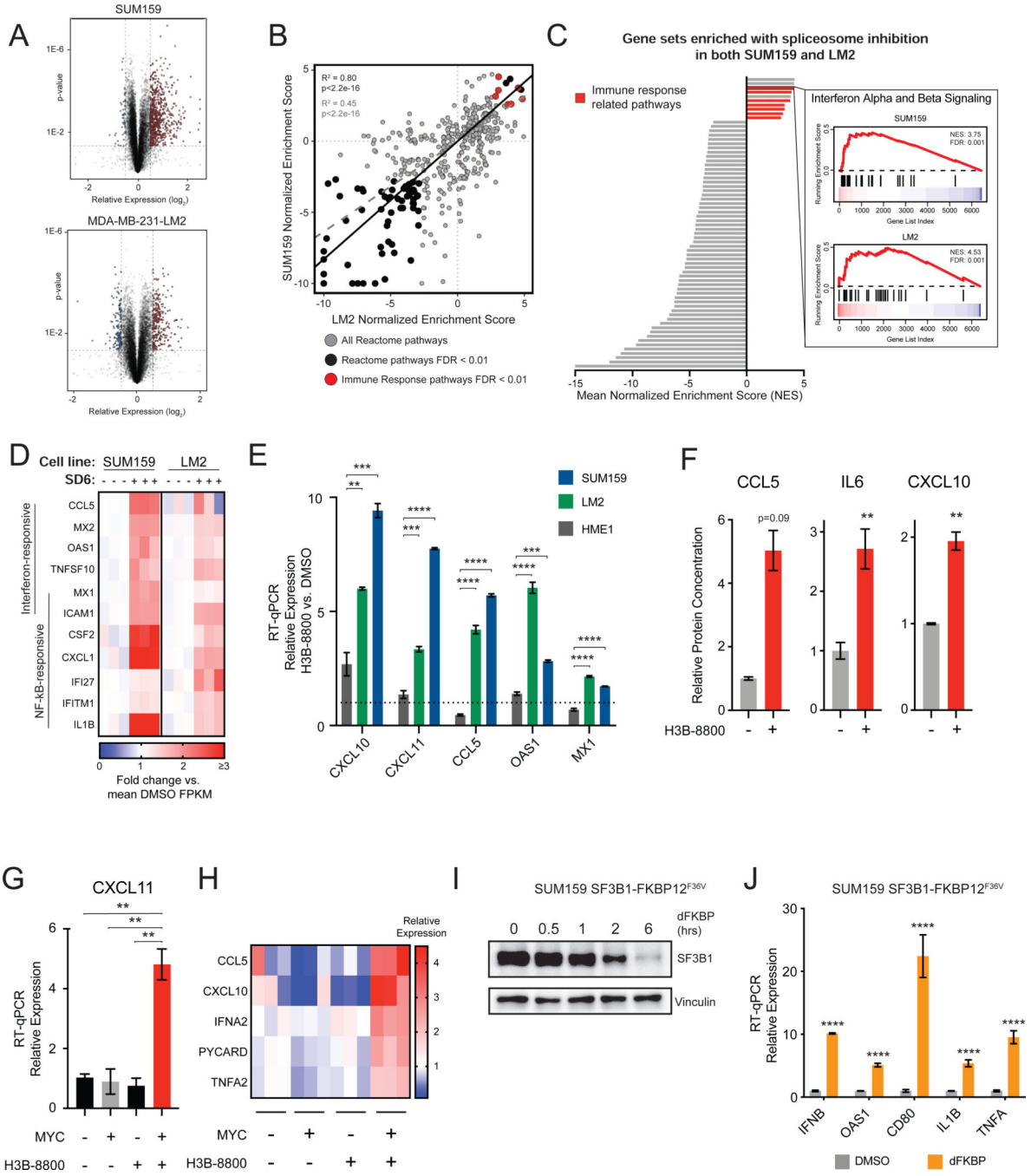

Figure 1. Spliceosome-Targeted Therapies Stimulate Antiviral Signaling in MYC-Driven Triple-Negative Breast Cancer

(A) Volcano plot of RNA-seq gene expression changes due to spliceosome inhibition for two MYC-driven TNBC cell lines, SUM159 and LM2, treated with SD6 or DMSO (n=3 biological replicates).

(B, C) Spliceosome inhibition leads to activation of immune signatures in MYC+ TNBC cells. (B) Scatterplot of gene sets enriched in SUM159 and LM2 after SD6 treatment. Gene sets with FDR <0.01 in both cell lines are black. Immune-related gene sets are red. Pearson correlation between all pathways shown as dashed gray line (R^2 =0.45, p<2.2e-16);

between pathways with FDR<0.01 as black line (R^2=0.80, p<2.2e-16). (C) Immune-related transcriptional pathways are among the most positively enriched. Gene sets with FDR <0.01 in both cell lines are shown, with immune-related gene sets in red (7 of 10 positively enriched pathways). The GSEA trace of Interferon Alpha and Beta Signaling is shown as an example.

(D) Spliceosome inhibition with SD6 leads to activation of interferon stimulated and NF-kB responsive genes. Heatmap of RNA-seq data shows relative expression (mean FPKM fold change vs. DMSO) of leading edge genes from enriched immune-related transcriptional pathways in panel (C).

(E) Spliceosome inhibition activates antiviral signaling in TNBC cells but not in non-transformed MECs. SUM159 and LM2 and non-transformed MECs (HME1) were treated with the same dose of H3B-8800. Gene expression assayed by RT-qPCR.

(F) Spliceosome inhibition leads to production of cytokines and chemokines. Conditioned media from SUM159 cells ± H3B-8800 was measured for CCL5, IL6, and CXCL10 (mean ± SEM, n=2 technical replicates, two-tailed unpaired Student's t-test).

(G, H) MYC hyperactivation primes antiviral transcriptional changes in response to spliceosome inhibition. HMECs with inducible MYC were treated ± 4-OHT (to induce MYC) ± H3B-8800. Transcription of (G) *CXCL11* and (H) other antiviral signaling targets was assayed by RT-qPCR.

(I, J) Chemical genetic degradation of SF3B1 upregulates interferon-stimulated and NF-kB responsive genes. SUM159s engineered with endogenous *SF3B1* knockout and exogenous *SF3B1-FKBP12*^{F36V} cDNA expression were (I) treated with dFKBP ligand to deplete SF3B1. (J) Gene expression assayed by RT-qPCR.

Bar plots of RT-qPCR data in (E), (G), and (J) are expressed relative to DMSO (mean ± SEM, n=3 biological replicates, two-tailed unpaired Student's t-test).

**p<0.01, ***p<0.001, **** p<0.0001. See also Figure S1.

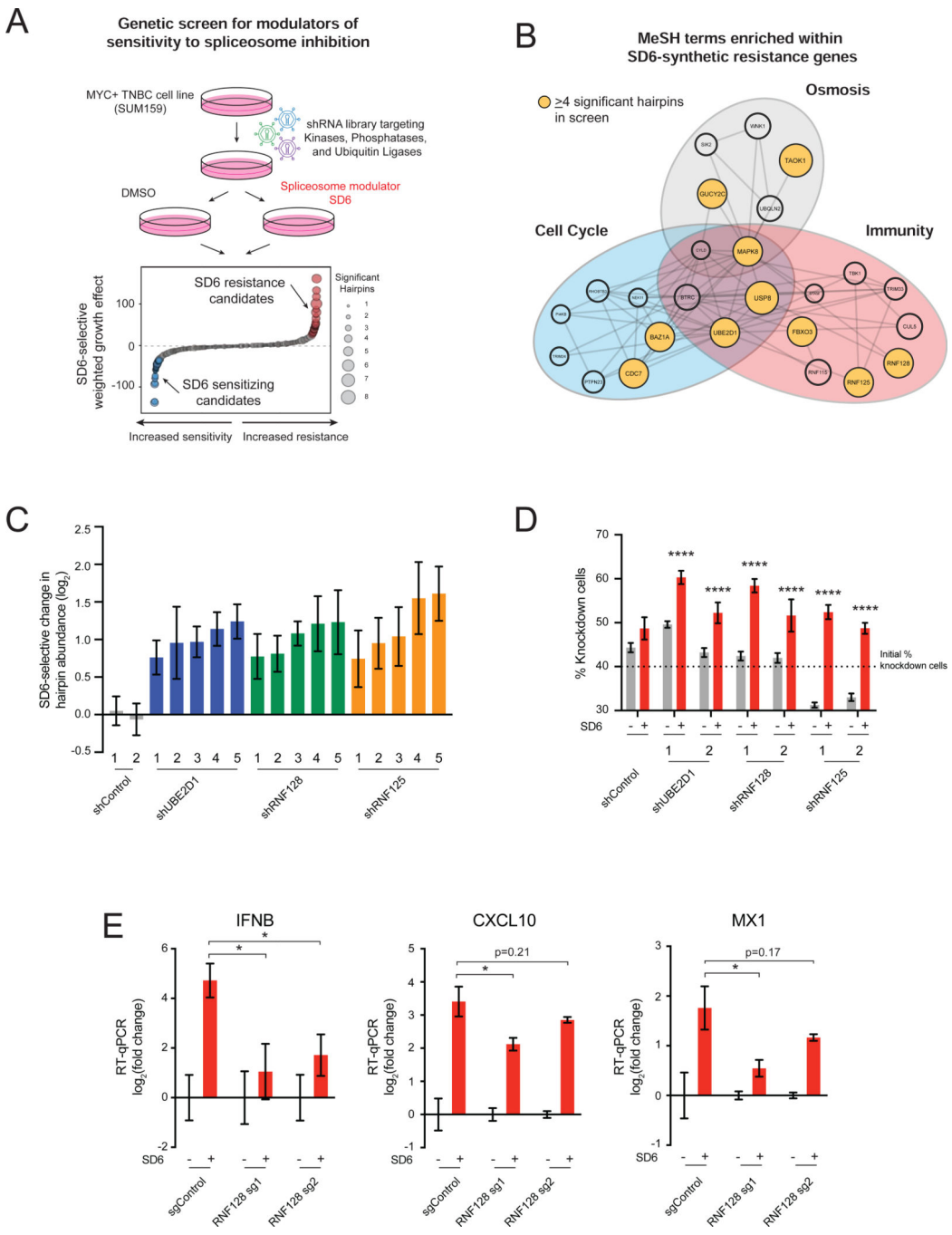

Figure 2. Components of Antiviral Response Pathways Modulate Sensitivity to Spliceosome Inhibition

(A, B) Immunity-related genes confer resistance to spliceosome inhibition. (A) shRNA screen for genes that modulate sensitivity to spliceosome-targeted therapies. SUM159 cells were transduced with an shRNA library and cultured ± SD6. Waterfall plot shows combined SD6-selective growth effect of each gene, calculated as a weighted effect of knockdown by multiple shRNAs. SD6 resistance candidates are red. SD6 sensitizing candidates are blue. (B) MeSH term enrichment analysis of top 50 resistance candidates. Enriched MeSH

terms (FDR<0.1) grouped by related function. Node size represents number of shRNAs that significantly conferred resistance (≥4 significant shRNAs highlighted in yellow).
(C, D) Knockdown of *UBE2D1*, *RNF128*, and *RNF125* confers resistance to spliceosome inhibition. (C) For each gene, the top five independent shRNAs from the screen are plotted along with two negative control shRNAs. $\log_2$ (fold change) calculated based on change in shRNA abundance in SD6 vs. DMSO (mean ± SEM, n=4 biological replicates). shRNAs with $\log_2$ (fold change) > 0.5 and p-value ≤ 0.05 shown. (D) SUM159 cells transduced with *RNF128*, *RNF125*, or *UBE2D1*-targeting or control shRNAs were mixed (40%) with SUM159-E2 Crimson cells (60%) and cultured ± SD6. Shown is the percentage of cells expressing a given shRNA for DMSO and SD6 treated samples (mean ± SEM, n=6 biological replicates, two-tailed unpaired Student's t-test).
(E) RNF128 is required for SD6-induced antiviral signaling. SUM159 cells expressing two RNA128-targeting or negative control sgRNAs were tested for expression of *IFNB*, *CXCL10*, and *MX1* ± SD6 treatment. Data shown as expression relative to DMSO (mean ± SEM, n=3 biological replicates, two-tailed unpaired Student's t-test).
*p<0.05, ****p<0.0001. See also Figure S2 and Tables S1 and S2.

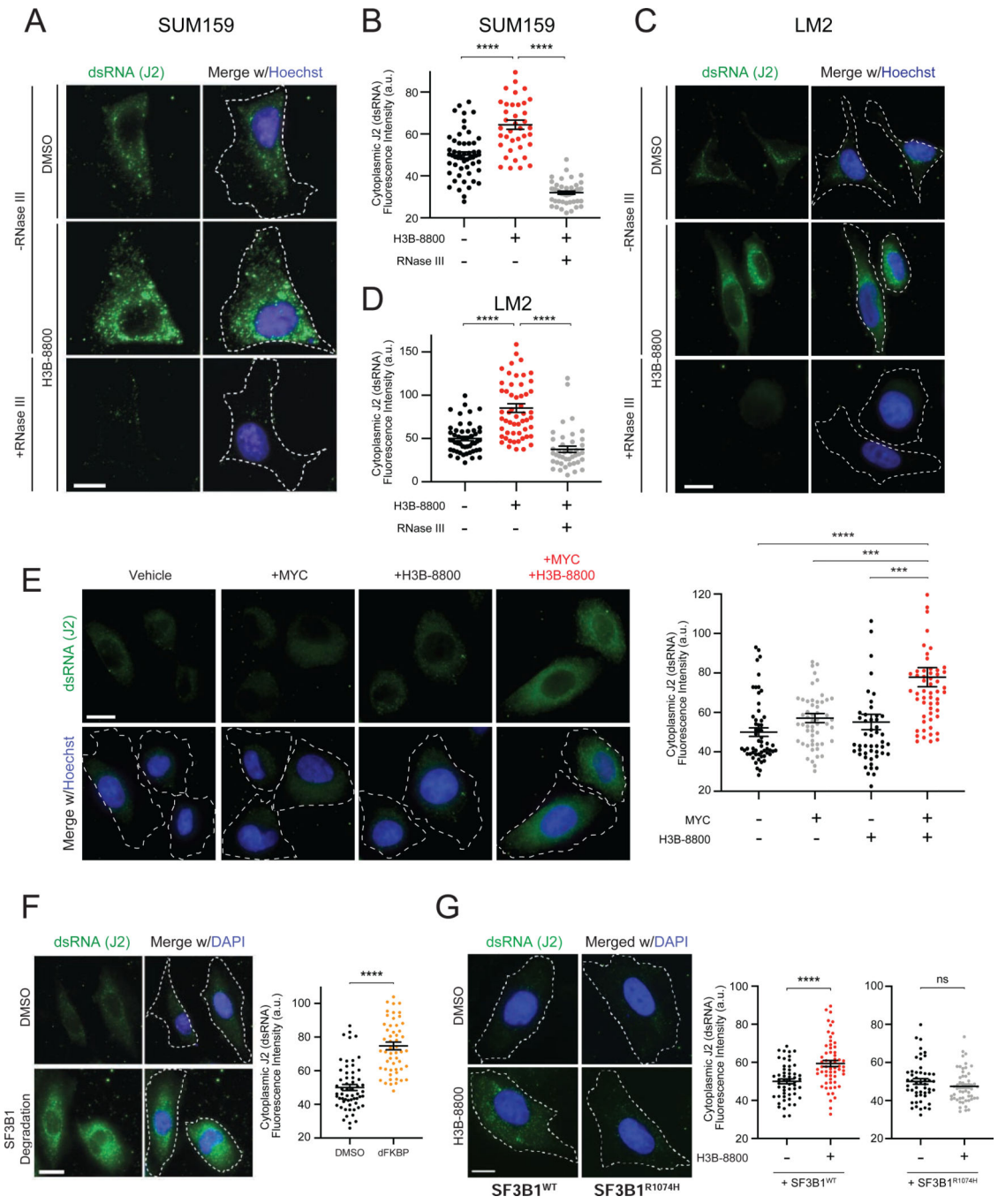

Figure 3. Spliceosome-Targeted Therapies Cause Cytoplasmic Accumulation of Double-stranded RNA (dsRNA) in TNBC Cells

(A-D) Spliceosome inhibition induces cytoplasmic dsRNA accumulation. (A, C) Cellular dsRNA was evaluated with anti-dsRNA (J2) immunofluorescence (IF) in (A) SUM159 and (C) LM2 cells ± H3B-8800. RNase III treatment used as negative control for dsRNA signal. Scale bars, 10μm. Images representative of 3 experiments. (B, D) Quantification of cytoplasmic dsRNA signal intensity for (B) SUM159 and (D) LM2.

(E) Spliceosome inhibition in combination with MYC hyperactivation induces cytoplasmic dsRNA accumulation. HMECs with inducible MYC were treated ± 4-OHT (to induce

MYC) ± H3B-8800 and assessed for dsRNA with J2 antibody. Scale bars, 10μm. Right, quantification of cytoplasmic dsRNA signal.

(F) SF3B1 degradation induces cytoplasmic dsRNA accumulation. Left, IF labeling of dsRNA (J2) in SUM159 SF3B1-FKBP12^{F36V} cells ± dFKBP. Images representative of 2 experiments. Scale bars, 20μm. Right, quantification of cytoplasmic dsRNA signal.

(G) Expression of spliceosome modulator-resistant SF3B1^{R1074H} mutant suppresses accumulation of dsRNA after H3B-8800 treatment. Left, IF labeling of dsRNA (J2) in SUM159 cells expressing SF3B1^{WT} and SF3B1^{R1074H} ± H3B-8800. Scale bars, 10μm. Right, quantification of cytoplasmic dsRNA signal.

All quantification plots of dsRNA signal intensity are mean ± SEM from >35 cells per group, two-tailed unpaired Student's t-test.

*p<0.05, ***p<0.001, ****p<0.0001. See also Figure S3.

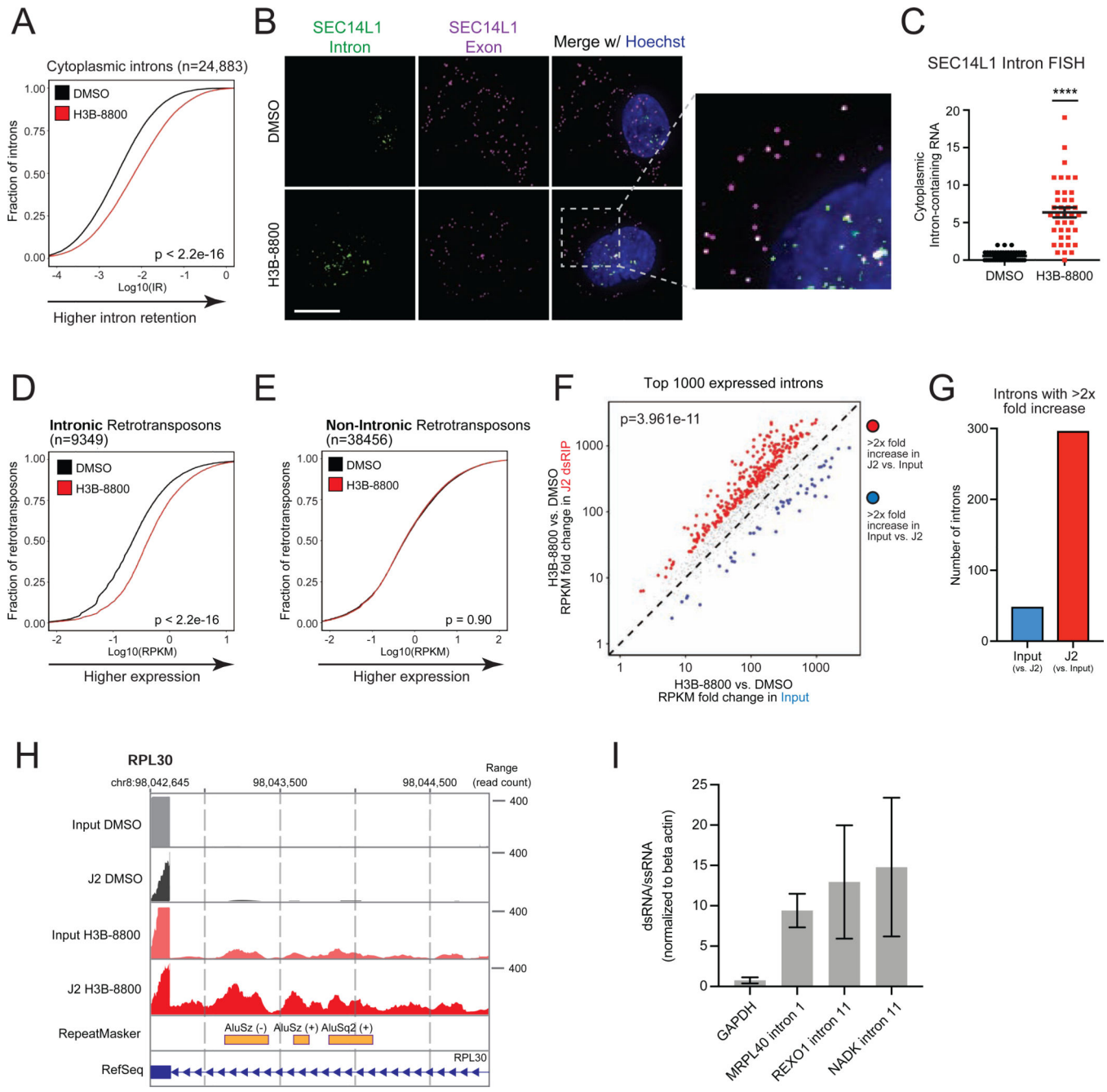

Figure 4. Intron-Retained RNAs Accumulate in the Cytoplasm and Form dsRNA in Response to Spliceosome-Targeted Therapies

(A-C) Spliceosome inhibition leads to cytoplasmic intron retention in TNBC cells. (A) RNA-seq was performed on cytoplasmic RNA from SUM159 ± H3B-8800 and intron retention (IR) was assessed. Empirical cumulative distribution curves of mean IR scores (n=2 biological replicates) shown. A rightward shift in the red curve indicates increased IR (p<2.2e-16, Mann-Whitney *U*). (B) RNA fluorescence *in situ* hybridization (FISH) images of retained introns and surrounding exon sequences for *SEC14L1* ± H3B-8800. Arrows indicate overlapped intron and exon foci. Scale bars, 10μm. (C) Quantification

of cytoplasmic intron-retained mRNAs per cell (mean ± SEM from >35 cells per group, two-tailed unpaired Student's t-test).

(D, E) Intron-residing retrotransposons increase in abundance in the cytoplasm of TNBC cells after H3B-8800. Empirical cumulative distribution curves of mean RPKMs are plotted for (D) 9,349 intron-residing retrotransposons or (E) 38,456 non-intronic retrotransposons detected in RNA-seq. A rightward shift in the red curve indicates increased expression in intronic retrotransposons ($p<2.2e-16$, Mann-Whitney *U*) but not non-intronic retrotransposons ($p = 0.90$, Mann-Whitney *U*).

(F, G, H) Retained introns induced by spliceosome inhibition form dsRNA. SUM159 cells ± H3B-8800 (n=2 biological replicates). dsRNA was enriched by J2 immunoprecipitation followed by poly(A) RNA-seq (J2 dsRIP-seq). (F) Scatterplot of intron expression fold changes ± H3B-8800 of the top 1000 introns ranked by expression (RPKM). (G) Number of retained introns with >2× increase in input or J2-dsRIP (compared to the other state). (H) Representative intron-embedded retrotransposons (*RPL30* gene).

(I) Introns retained after H3B-8800 form dsRNA structures. Lysates from SUM159 cells ± H3B-8800 were treated ± RNaseONE, a ssRNA specific ribonuclease. Relative RNA levels were quantified via RT-qPCR (mean ± SEM, n=3 biological replicates). Data shown are relative to *ACTB* mRNA, a well-characterized ssRNA.

****$p<0.0001$. See also Figure S4.

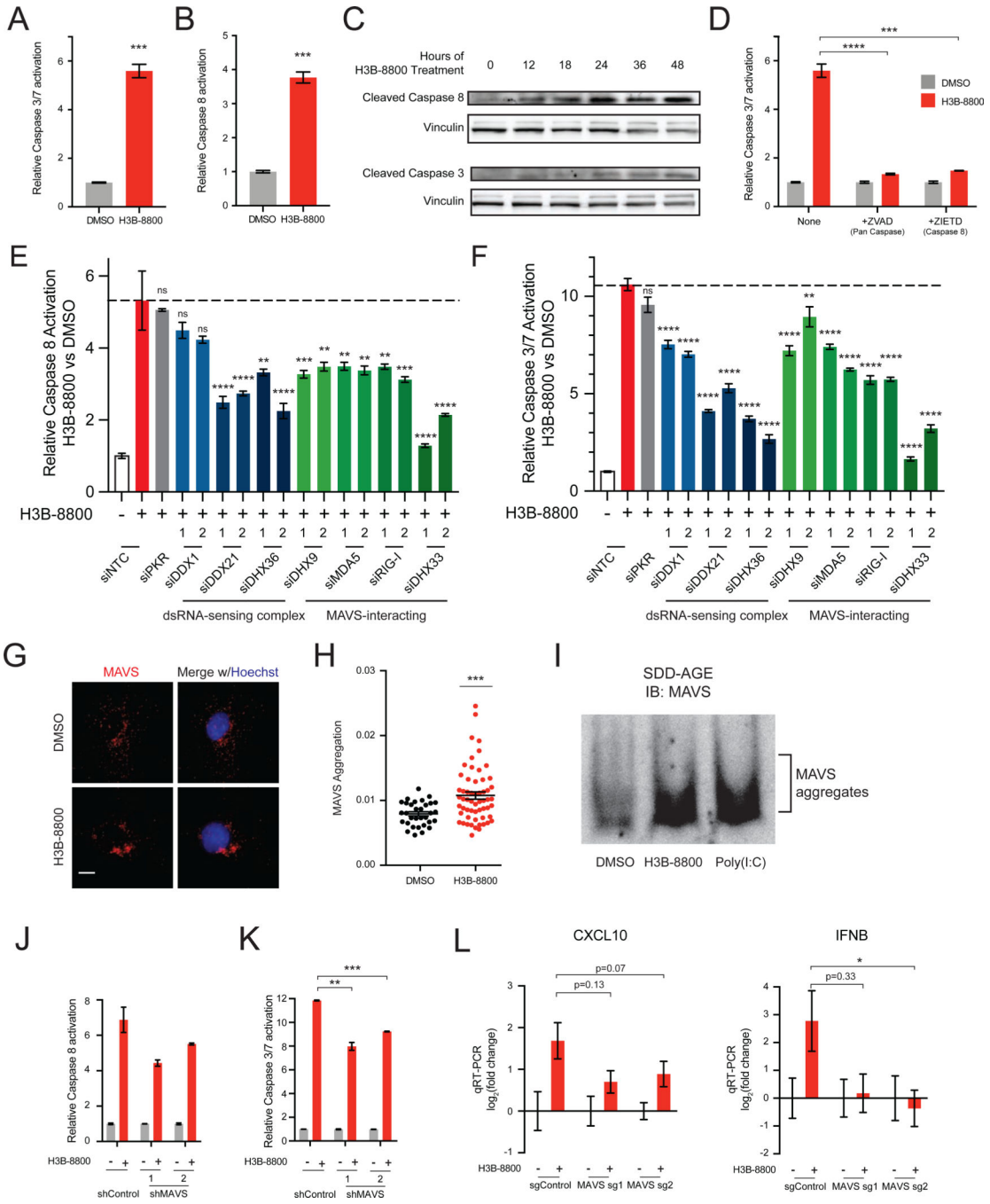

Figure 5. Spliceosome-Targeted Therapies Activate Extrinsic Apoptosis via Antiviral dsRNA Sensing Pathways

(A-D) Spliceosome inhibition activates apoptosis via extrinsic mechanisms. (A) Caspases-3 and −7 activity from SUM159s ± H3B-8800. (B) Caspase-8 activity from SUM159s ± H3B-8800. (C) Immunoblotting time course shows cleavage of caspase-8 precedes cleavage of caspase-3 in response to spliceosome inhibition in SUM159 cells. (D) H3B-8800-induced apoptosis requires the extrinsic initiator caspase-8. SUM159s ± H3B-8800 and no caspase inhibitor, pan-caspase inhibitor (ZVAD), or caspase-8 inhibitor (ZIETD) were measured for caspases-3 and −7.

(E, F) Multiple dsRNA sensors contribute to activation of extrinsic apoptosis and downstream effector caspases upon spliceosome inhibition. SUM159 cells were transfected with control (NTC) siRNA or siRNA targeting the indicated genes, treated ± H3B-8800, and assessed for (E) caspase-8 and (F) caspases-3 and −7 (mean ± SEM, n≥3 biological replicates, one-way ANOVA with Dunnett's multiple comparison test).

(G-I) Spliceosome inhibition causes aggregation of the mitochondrial antiviral signaling protein MAVS. (G) MAVS immunofluorescence (IF) of SUM159 cells ± H3B-8800. Scale bars, 10μm. (H) MAVS aggregation quantified by inverse dispersal of IF signal (mean ± SEM, two-tailed unpaired Student's t-test). (I) P5 mitochondrial fraction was prepared from SUM159 cells ± H3B-8800 or transfected with poly (I:C). MAVS aggregation analyzed by SDD-AGE.

(J, K) Knockdown of *MAVS* suppresses activation of extrinsic apoptosis and downstream effector caspases upon spliceosome inhibition. SUM159 cells expressing control or MAVS-targeted shRNA were treated ± H3B-8800 and assessed for (J) caspase-8 and (K) caspases-3 and −7 (mean ± SEM, n=2 biological replicates, two-tailed unpaired Student's t-test).

(L) *MAVS* knockout suppresses upregulation of antiviral signaling in TNBC cells treated with H3B-8800. SUM159 cells expressing two independent *MAVS* sgRNAs assessed for *CXCL10* and *IFNB* expression ± H3B-8800. Data shown relative to DMSO (mean ± SEM, n=3 biological replicates, two-tailed unpaired Student's t-test).

Bar plots in panels (A), (B), and (D) of caspase activity shown as mean ± SEM, n=3 biological replicates, two-tailed unpaired Student's t-test.

*p<0.05, **p<0.01, ***p<0.001, ****p<0.0001. See also Figure S5.

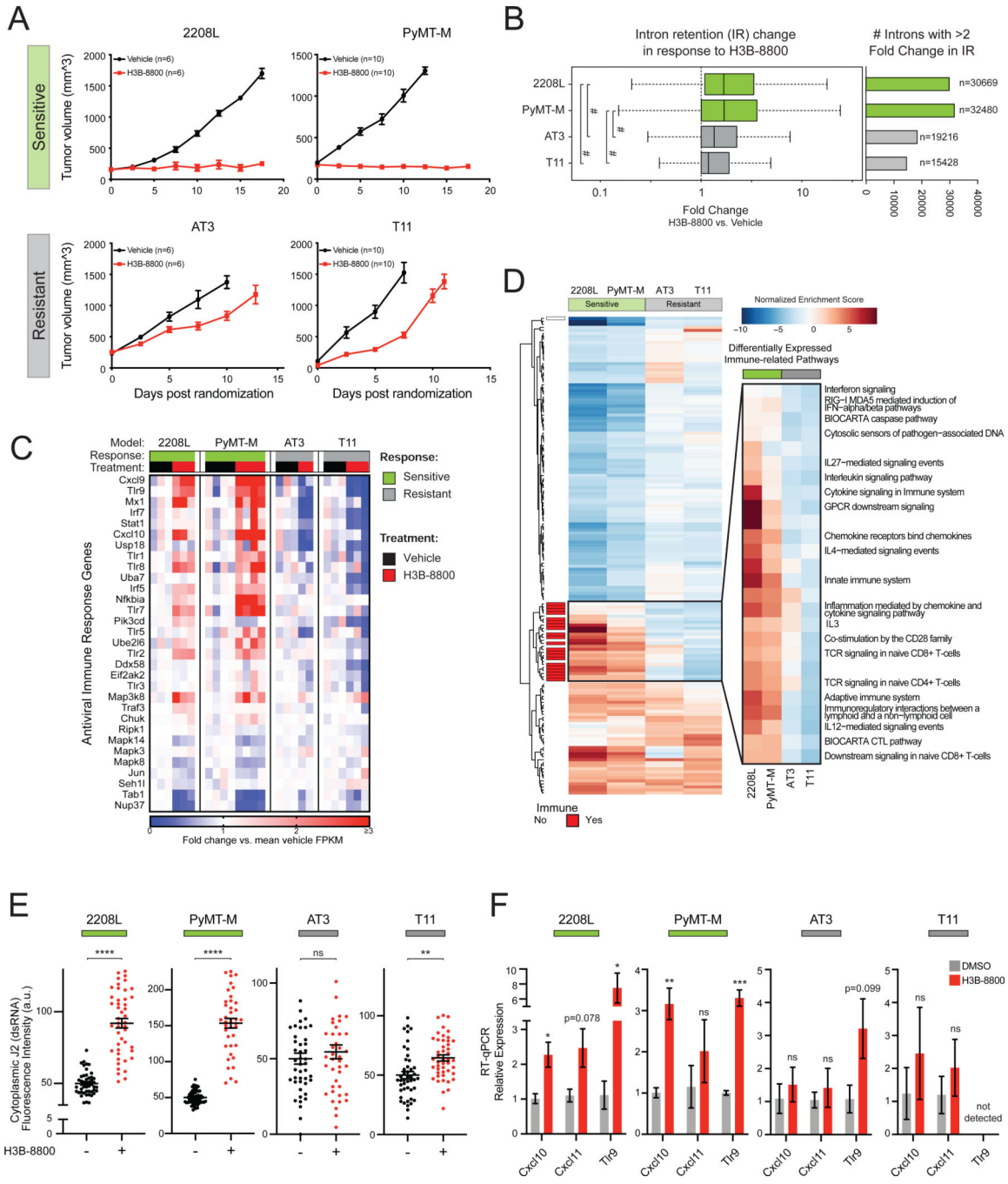

Figure 6. RNA Splicing Inhibition Induces Antiviral and Adaptive Signaling in Immune Competent Models of Breast Cancer

(A) H3B-8800 impairs tumor progression heterogeneously across syngeneic murine TNBC tumor models. 2208L and PyMT-M tumor progression was significantly impaired (termed sensitive), while AT3 and T11 tumors progressed (termed resistant) (mean ± SEM number of animals plotted).

(B) H3B-8800 results in higher global intron retention in sensitive tumor models ($p<2.2e-16$, Mann-Whitney *U*). Boxplot (left) of transcriptome-wide IR scores. Bar plot (right) indicates number of introns with >2-fold change in IR in H3B-8800 vs. Vehicle-treated tumors.

(C) H3B-8800 stimulates expression of antiviral signaling genes in sensitive tumor models. Genes shown are part of KEGG and Reactome antiviral signaling-related pathways. Relative expression calculated as mean FPKM fold change vs. vehicle.
(D) Immune pathways are strongly induced by H3B-8800 in sensitive tumor models but not in resistant tumor models. Pathways shown from MSigDB C2 Canonical Pathways have GSEA FDR<0.05 in either both of the sensitive or both of the resistant models. Immune pathways (red) are annotated based on leading edge genes.
(E) Spliceosome inhibition leads to accumulation of cytoplasmic dsRNA in sensitive syngeneic models of TNBC *in vitro*. Cell lines derived from syngeneic mouse TNBC models were assessed for cytoplasmic dsRNA using J2-immunofluorescence. Quantification of cytoplasmic dsRNA signal intensity shown (mean ± SEM from ≥40 cells per group, two-tailed unpaired Student's t-test).
(F) H3B-8800 induces transcriptional activation of antiviral immune signaling in sensitive syngeneic models of TNBC *in vitro*. Cell lines were treated with H3B-8800 and immune transcriptional activation was measured via RT-qPCR. Data are relative to DMSO (mean ± SEM, n=3 biological replicates, two-tailed unpaired Student's t-test).
*p<0.05, **p<0.01, ***p<0.001, ****p<0.0001, #p<2.2e-16. See also Figure S6 and Table S3.

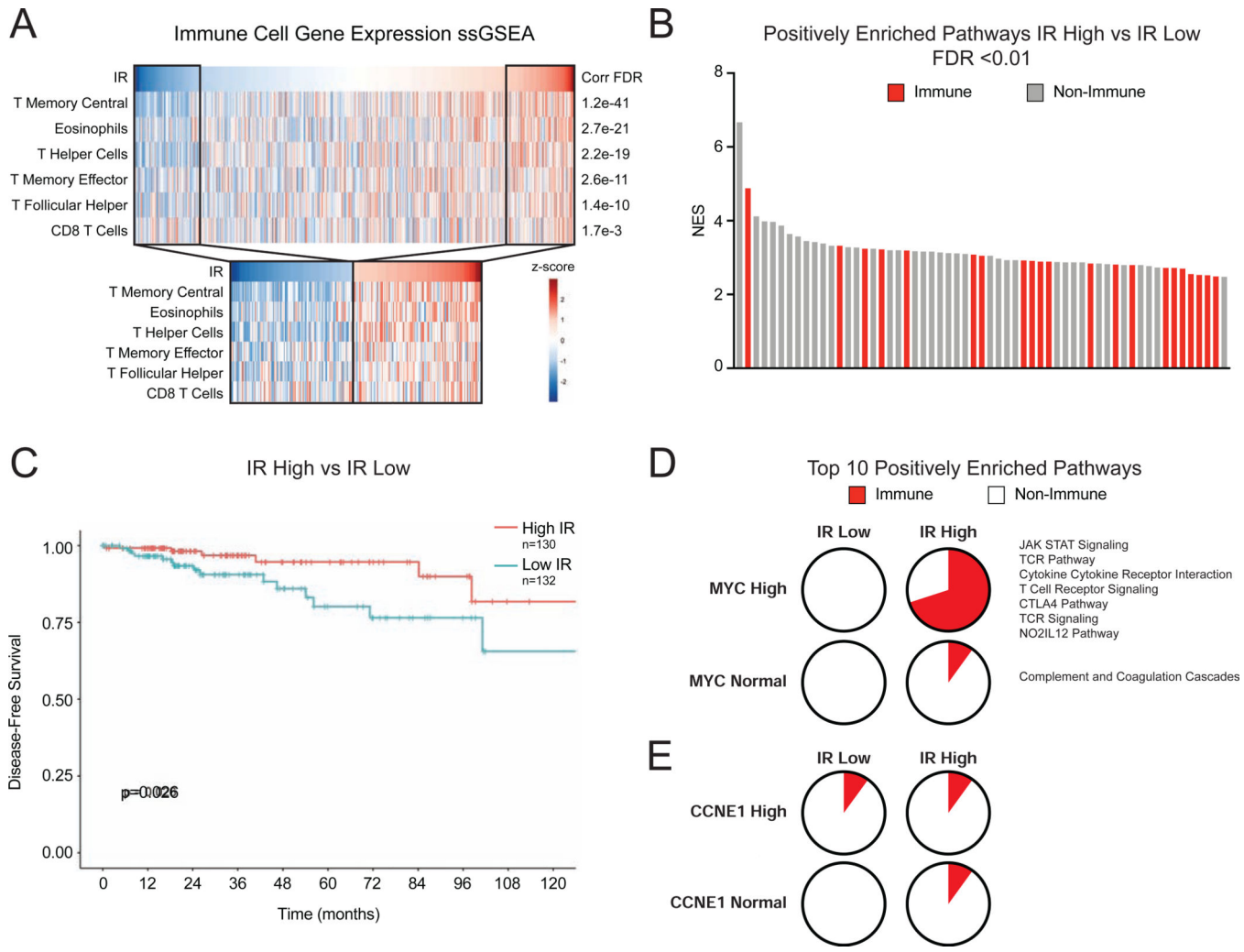

Figure 7. Defects in RNA Splicing and MYC Amplification Associate with Immune Response in Human Breast Cancer

(A) Intron retention (IR) correlates with signatures of immune infiltration in human breast cancer. Scores from ssGSEA analysis of immune cell gene signatures were computed and correlated to IR levels in BRCA tumors (n=983) in TCGA. Heatmaps show IR level across tumors and ssGSEA scores for signatures that have Pearson correlation q-value of <0.01, ranked by q-value. Subset heatmaps show tumors with IR level >1 z-score from the mean.

(B) Immune-related gene sets are enriched in tumors with high IR. GSEA with MSigDB C2 Canonical Pathways was used to compare gene expression of tumors with high vs. low IR (>1 z-score from mean). Bar plot of NES of positively enriched gene sets (FDR <0.01). Red indicates immune-related gene set.

(C) Tumors with high IR have improved disease-free survival (DFS). Kaplan-Meier plot shows DFS for patients with breast tumors (TCGA). High IR tumors have improved DFS (p=0.026, log-rank test).

(D, E) MYC-amplified breast tumors exhibit increased IR-associated immune signaling pathway activity. GSEA was used to compare gene expression patterns of human tumors divided into cohorts based on IR levels and MYC amplification. (D) Pie charts represent the

percent of immune-related pathways among the top 10 enriched pathways ranked by NES. In the High IR, High MYC cohort, 7 of 10 pathways are related to immune signaling. (E) In comparison, CCNE1 amplified tumors do not exhibit increased IR-associated immune signaling.

See also Figure S7 and Table S4.

KEY RESOURCES TABLE

REAGENT or RESOURCE	SOURCE	IDENTIFIER
Antibodies		
Rabbit polyclonal anti-SF3B1	Bethyl	Cat#A300–996A
Mouse monoclonal anti-Vinculin	Sigma	Cat#V9131
Mouse monoclonal anti-FLAG M2	Sigma	Cat#F1804
Mouse monoclonal anti-βActin	Sigma	Cat#A1978
Mouse monoclonal anti-αTubulin DM1A	Cell Signaling	Cat#3873
Rabbit polyclonal anti-H3	Millipore	Cat#07–690
Rabbit monoclonal anti-Cleaved Caspase 8 18C8	Cell Signaling	Cat#9496
Rabbit polyclonal anti-Cleaved Caspase 3	Cell Signaling	Cat#9661
Mouse monoclonal anti-RAN Clone 20	BD Biosciences	Cat#610340
Rabbit monoclonal anti-DR5 D4E9	Cell Signaling	Cat#8074
Rabbit polyclonal anti-TNFR2	Cell Signaling	Cat#3727
Rabbit monoclonal anti-DR4 D9S1R	Cell Signaling	Cat#42533
Rabbit monoclonal anti-TNFR1 C25C1	Cell Signaling	Cat#3736
Rabbit monoclonal anti-DR6 E8D21	Cell Signaling	Cat#93026
Rabbit monoclonal anti-cFLIP D5J1E	Cell Signaling	Cat#56343
Rabbit polyclonal anti-MAVS	Cell Signaling	Cat#3993
Mouse monoclonal J2 (anti-dsRNA)	Scicons	Cat#10010500
Alexa Fluor 488 goat anti-mouse IgG	Invitrogen	Cat#A11029
Alexa Fluor 594 goat anti-rabbit IgG	Invitrogen	Cat#A11012
Rabbit monoclonal anti-CD8a D4W2Z	Cell Signaling	Cat#98941
Bacterial and Virus Strains		
N/A	N/A	N/A
Biological Samples		
Syngeneic mouse tumors	Laboratory of Xiang H.-F. Zhang	N/A
Chemicals, Peptides, and Recombinant Proteins		
H3B-8800	Seiler et al., 2018	N/A
SD6	Lagisetti et al., 2013	N/A
dTAG-51	Nabet et al., 2018	N/A
Z-VAD-FMK	R&D Systems	Cat#FMK001
Z-IETD-FMK	R&D Systems	Cat#FMK007
Z-AEVD-FMK	R&D Systems	Cat#FMK009
Z-LEHD-FMK	R&D Systems	Cat#FMK008
RNase III	Applied Biosystems	Cat#A2290

REAGENT or RESOURCE	SOURCE	IDENTIFIER
RNaseOne	Promega	Cat#M4261
SuperScript III	ThermoFisher Scientific	Cat#18080093
SYBR Select Master Mix	Applied Biosciences	Cat#4472908
Hoechst 33342, trihydrochloride, trihydrate	Life Technologies	Cat#H3570
Protease Inhibitor Cocktail	Roche	Cat#11836170001
Phosphatase Inhibitor Cocktail 2	Sigma	Cat#P5726
Clarity ECL Substrate	Bio-Rad	Cat#170–5060
Q5 High-Fidelity 2X MasterMix	New England Biosciences	Cat#M04292
RNasin Plus	Promega	Cat#N2111
Protein A Dynabeads	Invitrogen	Cat#10001D
Propidium Iodide	Sigma Aldrich	Cat#P4864
Critical Commercial Assays		
RT^2 Profiler PCR Array Human Antiviral Response	Qiagen	Cat#330321
Milliplex Human Cytokine/Chemokine Panel 1	MilliporeSigma	Cat#HCYTOMAG-60K
CellTiterGlo	Promega	Cat#G7570
Caspase-Glo 3/7	Promega	Cat#G8090
Caspase-Glo 8	Promega	Cat#G8200
Pierce BCA Protein Assay	Thermo Scientific	Cat#23225
Deposited Data		
SUM159 SD6 RNA-Seq	This manuscript	GEO#GSE163414
LM2 SD6 RNA-Seq	This manuscript	GEO#GSE163411
SUM159 Cytoplasmic RNA-Seq	This manuscript	GEO#GSE163232
SUM159 J2 dsRIPseq	This manuscript	GEO#GSE163188
Syngeneic model RNA-Seq	This manuscript	GEO#GSE163181
TCGA RNA-Seq Data	Koboldt et al., 2012	dbGaP: phs000178.v10.p8; https://www.ncbi.nlm.nih.gov/projects/gap/cgi-bin/study.cgi?study_id=phs000178.v10.p8
TCGA RNA-Seq Clinical Data	The Cancer Genome Atlas Research Network	https://portal.gdc.cancer.gov/
Experimental Models: Cell Lines		
Human: 293T	ATCC	Cat#ATCC CRL-3216
Human: SUM159 (female)	BioIVT	Cat#SUM-159PT

REAGENT or RESOURCE	SOURCE	IDENTIFIER
Human: MDA-MB-231-LM2 (female)	Minn et al., 2005	N/A
Human: HME1 (female)	Infinity	Cat#hTERT-HME1
Human: HME1 MYC-ER	Kessler et al., 2012	N/A
Human: SUM159 *SF3B1*$^{-/-}$ SF3B1-FKBP12^{F36V}	This manuscript	N/A
Human: MDA-MB-231 (female)	ATCC	Cat#ATCC HTB-122
Human: BT549 (female)	ATCC	Cat#ATCC HTB-26
Human: SUM159 SF3B1^{WT}	This manuscript	N/A
Human: SUM159 SF3B1^{R1074H}	This manuscript	N/A
Human: MDA-MB-231-LM2 SF3B1^{WT}	This manuscript	N/A
Human: MDA-MB-231-LM2 SF3B1^{R1074H}	This manuscript	N/A
Mouse: p53$^{-/-}$ 2208L (female)	Laboratory of Xiang H.-F. Zhang	N/A
Mouse: p53$^{-/-}$ T11 (female)	Laboratory of Xiang H.-F. Zhang	N/A
Mouse: MMTV PyMT-M (female)	Laboratory of Xiang H.-F. Zhang	N/A
Mouse: AT3 (female)	Laboratory of Xiang H.-F. Zhang	N/A
Experimental Models: Organisms/Strains		
Mouse: BALB/c AnNHsd (female)	Envigo	Cat#4701F
Mouse: C57BL/6J (female)	Jackson Laboratory	Cat#000664
Oligonucleotides		
See Table S5 for shRNA sequences	Rousseaux et al., 2018	N/A
See Table S5 for siRNA sequences	ThermoFisher	https://www.thermofisher.com/us/en/home/life-science/rnai/synthetic-rnai-analysis/ambion-silencer-select-sirnas.html
See Table S6 for Primer Sequences used for RT-qPCR	Integrated Data Technologies	N/A
See Table S7 for smFISH probe sequences	Biosearch Technologies, Inc.	N/A
shRNA Genomic Amplification Forward Primer: TCGTCGGCAGCGTCAGATGTGTATAAGAGACAGTAGTGAAGCCACAGATGTA	Integrated Data Technologies	N/A
shRNA Genomic Amplification Reverse Primer: GTCTCGTGGGCTCGGAGATGTGTATAAGAGACAGTATAAACGGTTGGTCTTCCAA	Integrated Data Technologies	N/A

REAGENT or RESOURCE	SOURCE	IDENTIFIER
sgRNA Control Sequence: GTCCTGGCAGGGCTGTGGTG	ThermoFisher	https://www.thermofisher.com/us/en/home/life-science/genome-editing/geneart-crispr/crispr-libraries/lentiarray-crispr-libraries.html
RNF128 sgRNA-1 Sequence: CACGAATTTCACGGTGCCCA	ThermoFisher	https://www.thermofisher.com/us/en/home/life-science/genome-editing/geneart-crispr/crispr-libraries/lentiarray-crispr-libraries.html
RNF128 sgRNA-2 Sequence: GAAATTCGTGTGCGGGTTAC	ThermoFisher	https://www.thermofisher.com/us/en/home/life-science/genome-editing/geneart-crispr/crispr-libraries/lentiarray-crispr-libraries.html
MAVS sgRNA-1 Sequence: GTACTTCATTGCGGCACTGA	ThermoFisher	https://www.thermofisher.com/us/en/home/life-science/genome-editing/geneart-crispr/crispr-libraries/lentiarray-crispr-libraries.html
MAVS sgRNA-2 Sequence: GGGTATTGAAGAGATGCCAG	ThermoFisher	https://www.thermofisher.com/us/en/home/life-science/genome-editing/geneart-crispr/crispr-libraries/lentiarray-crispr-libraries.html
SF3B1 crRNA-1 Sequence: AAGAUCGCCAAGACUCACGA	Dharmacon	Cat#CR-020061–01
Edit-tracrRNA	Dharmacon	Cat#U-002000
Recombinant DNA		
pINDUCER20-Cas9	This manuscript	N/A
pHAGE-PGK-E2 Crimson	This manuscript	N/A
pHAGE-PGK-SF3B1-FKBP12^{F36V}	This manuscript	N/A
pINDUCER20-SF3B1^{WT}	This manuscript	N/A
pINDUCER20-SF3B1^{R1074H}	This manuscript	N/A
pCW-Cas9	Wang et al., 2014	Addgene (Plasmid #50661)
pInducer20	Meerbrey et al., 2011	Addgene (Plasmid #44012)
Software and Algorithms		
SAMtools (v1.4)	Li et al., 2009	https://github.com/samtools/
Hisat2 (v2.0.4)	Kim et al., 2015	https://daehwankimlab.github.io/hisat2/

REAGENT or RESOURCE	SOURCE	IDENTIFIER
Cufflinks (v2.2.1)	Trapnell et al., 2010	https://github.com/cole-trapnell-lab/cufflinks
FeatureCounts (v1.6.2)	Liao et al., 2014	http://subread.sourceforge.net/
MSigDB	Subramanian et al., 2005; Liberzon et al., 2011	http://www.broadinstitute.org/gsea/msigdb
Mouse gene expression pathways	Baderlab	http://baderlab.org/GeneSets
RefSeq Annotation	NCBI	https://www.ncbi.nlm.nih.gov/refseq/
DESeq2	Love et al., 2014	https://bioconductor.org/packages/release/bioc/html/DESeq2.html
Pysam	Li et al., 2009	https://github.com/pysam-developers/pysam
RepeatMasker (open-4.0.5)	Institute for Systems Biology	http://www.repeatmasker.org/
Metascape	Zhou et al., 2019	https://metascape.org/gp/index.html#/main/step1
Cutadapt	Martin, 2011	https://cutadapt.readthedocs.io/en/stable/index.html
Bowtie2	Langmead and Salzberg, 2012	https://github.com/BenLangmead/bowtie2
Meshes (v1.8.0)	Yu, 2018	https://bioconductor.org/packages/release/bioc/html/meshes.html
StringDB (v11.0)	Szklarczyk et al., 2018	https://string-db.org/
NIS-Element AR	Nikon	AR 4.30.01
ImageJ	NIH	https://imagej.nih.gov/ij/index.html
RNAfold	Institute for Theoretical Cehmistry	http://rna.tbi.univie.ac.at/cgi-bin/RNAWebSuite/RNAfold.cgi
Adobe Photoshop	Adobe	N/A
ssGSEA	Barbie et al., 2009	https://github.com/broadinstitute/ssGSEA2.0
STAR aligner (v2.3.1)	Dobin et al., 2013	https://github.com/alexdobin/STAR
TCGAbiolinks	Colaprico et al., 2015	https://bioconductor.org/packages/release/bioc/html/TCGAbiolinks.html
Other		
N/A	N/A	N/A